



UPPSALA  
UNIVERSITET

*Digital Comprehensive Summaries of Uppsala Dissertations  
from the Faculty of Science and Technology 2016*

# Computational Insights into Atomic Scale Wear Processes in Cemented Carbides

EMIL EDIN



ACTA  
UNIVERSITATIS  
UPSALIENSIS  
UPPSALA  
2021

ISSN 1651-6214  
ISBN 978-91-513-1140-1  
urn:nbn:se:uu:diva-434522

Dissertation presented at Uppsala University to be publicly examined in Polhemsalen, Ångströmlaboratoriet, Lägerhyddsvägen 1, Uppsala, Wednesday, 31 March 2021 at 13:00 for the degree of Doctor of Philosophy. The examination will be conducted in English. Faculty examiner: Professor Hannes Jónsson (University of Iceland).

### Abstract

Edin, E. 2021. Computational Insights into Atomic Scale Wear Processes in Cemented Carbides. *Digital Comprehensive Summaries of Uppsala Dissertations from the Faculty of Science and Technology* 2016. 76 pp. Uppsala: Acta Universitatis Upsaliensis. ISBN 978-91-513-1140-1.

As Ti-alloys become more and more utilized the need for efficient and robust manufacturing of Ti-alloy components increase in importance. Ti-alloys are more difficult to machine than e.g. steel, mainly due to their poor thermal conductivity leading to rapid tool wear. The atomic scale processes responsible for this wear is not well understood. Here the focus is turned to the effects of C diffusion out of the tools as a source of the observed wear. A combination of Density Functional Theory (DFT) making use of Harmonic Transition State Theory (HTST), classical Molecular Dynamics (MD) and kinetic Monte Carlo (kMC) is used to investigate C diffusion into and within experimentally observed WC/W interfaces that exists as a consequence of the C depletion. Further, tools are built and used to evaluate interface parameters for large sets of interfaces within the WC/W system to determine which are energetically preferred. The results from the DFT study show stable interfaces with large differences in activation energy between the two most prominent surfaces found in WC materials, namely the basal and prismatic surfaces. Within the WC/W interfaces the diffusion barriers are similar between the two. The classical MD simulations support the view of stable interfaces at the early stages of C depletion. As C is removed this picture shifts to one in which the diffusion barriers are substantially decreased and the difference between the basal and the prismatic interfaces vanish pointing to a process which starts out slow but accelerates as C is continually removed. From the kMC simulations the overall diffusion pre-factor and activation energy is estimated to be  $D_0 = 1.8 \times 10^{-8} \text{ m}^2/\text{s}$  and  $dE = 1.24 \text{ eV}$  for the investigated  $[10\text{-}10]\text{-I}[100]$  interface, the kMC simulations also confirm previous results indicating that the diffusion is restricted to the interface region. The investigation and screening of properties for WC/W interfaces show a preference for the W terminated  $[10\text{-}10]\text{-I}[110]$  and  $[0001]/[110]$  interface combinations based on the interfacial energy.

**Keywords:** WC, Cemented Carbides, Diffusion, Wear, Interfaces

*Emil Edin, Department of Physics and Astronomy, Materials Theory, Box 516, Uppsala University, SE-751 20 Uppsala, Sweden.*

© Emil Edin 2021

ISSN 1651-6214

ISBN 978-91-513-1140-1

urn:nbn:se:uu:diva-434522 (<http://urn.kb.se/resolve?urn=urn:nbn:se:uu:diva-434522>)

*Dedicated to my dad,  
a soon to be retired math and physics teacher.*



# List of papers

This thesis is based on the following papers, which are referred to in the text by their Roman numerals.

- I **First principles study of C diffusion in WC/W interfaces observed in WC/Co tools after Ti-alloy machining.** E. Edin, W. Luo, R. Ahuja, B. Kaplan, A. Blomqvist, *Computational Material Science*, 2019, 161, 236-243
- II **MD study of C diffusion in WC/W interfaces observed in cemented carbides.** E. Edin, A. Blomqvist, M. Lattemann, W. Luo, R. Ahuja, *International Journal of Refractory Metals & Hard Materials*, 2019, 85, 105054
- III **interfaceBuilder, a python tool for building and analyzing interfaces suitable for use in large screening applications.** E. Edin, A. Blomqvist, M. Lattemann, W. Luo, R. Ahuja, (*Submitted*)
- IV **Large scale screening of interface parameters in the WC/W system using classical force field and first principles calculations.** E. Edin, A. Blomqvist, W. Luo, R. Ahuja, *Journal of Physical Chemistry C*, 2021
- V **Study of C diffusion in WC/W boundaries using Adaptive Kinetic Monte Carlo.** E. Edin, A. Blomqvist, W. Luo, R. Ahuja, (*Manuscript*)

Reprints were made with permission from the publishers.

## Comments on my own contributions

In all papers and manuscript I have in large part been responsible for the computational design of the projects and carried out the practical execution i.e. calculations and creation of specific analysis tools as needed. I have been responsible for the majority of the analysis and writing for all manuscripts as well as the handling of all submissions.



# Contents

1	Introduction .....	9
2	Computational Background .....	12
2.1	Density Functional Theory .....	12
2.1.1	Many-Body Description .....	12
2.1.2	Born-Oppenheimer Approximation .....	13
2.1.3	Electron Density Approach .....	13
2.1.4	Exchange and Correlation Functionals .....	15
2.1.5	Self Consistent Field .....	15
2.1.6	Basis Sets .....	16
2.1.7	Plane Waves .....	17
2.1.8	Pseudopotentials and Projector Augmented Wave Method .....	17
2.1.9	Forces .....	18
2.2	Classical Force Fields .....	18
2.2.1	Concept .....	19
2.2.2	Analytical Bond Order Potential .....	20
2.3	Molecular Dynamics .....	22
2.3.1	Radial Distribution Function .....	23
2.3.2	Mean Square Displacement .....	23
2.4	Kinetic Monte Carlo .....	24
3	Diffusion, Surfaces and Interfaces .....	26
3.1	Atomistic Diffusion .....	26
3.2	Harmonic Transition State Theory .....	27
3.3	Nudge Elastic Band .....	28
3.4	Dimer .....	29
3.5	Surfaces .....	30
3.6	Interfaces .....	32
4	Cemented Carbides in Metal Machining .....	33
4.1	Cemented Carbides .....	33
4.2	Ti-Alloys .....	33
4.3	Ti-Alloy Machining .....	35
5	DFT Study of C Diffusion in WC/W Interfaces .....	37
5.1	Computational Approach .....	37
5.2	Results and Discussion .....	39

6	MD Simulations of C Diffusion as a Function of C Depletion .....	43
6.1	Computational Approach .....	43
6.2	Results and Discussion .....	45
7	Tools for Finding, Building and Analysing Interfaces .....	48
7.1	Concept .....	48
7.2	Application and Capabilities .....	49
8	Large Scale Screening of WC/W Interface Parameters .....	54
8.1	Computational Approach .....	54
8.2	Results and Discussion .....	56
9	KMC Simulations of C Diffusion .....	61
9.1	Computational Approach .....	61
9.2	Results .....	62
10	Summary and Outlook .....	66
11	Acknowledgements .....	69
12	Svensk Sammanfattning .....	70



# 1. Introduction

In a fast-evolving world where technological innovation is needed to solve the great issues of our time and improve our lives on a day to day basis the demand for high performance materials is steadily increasing. From Light weight alloys to reduce fuel consumption and minimize losses to structurally stable materials at high temperatures to allow for efficiency increases to materials better able to withstand corrosive environments or materials for use in medical implants, many breakthroughs are made possible by the properties of speciality materials.

One material that is often mentioned when talking advanced applications is Ti, with a reputation making the name alone enough to sell products at premium markups within some fields e.g. recreational equipment etc. Within industrial applications though, Ti and Ti-alloys are used for good reason as properties include good strength to weight ratio, good high temperature strength and corrosion resistance to name a few. Due to this it is widely used within several advanced fields including aerospace, top end automotive, chemical manufacturing, medical implants, military applications [1–5] and naturally really expensive camping equipment. An interesting point of reference is the increase of Ti-alloys in commercial airliners which has gone from 1% of the total empty weight for planes rolled out in the 60's to as much as 19% for planes rolled out in the last decade [4].

Though the upsides to using Ti-alloys are many the downside is often price which is evidenced by the areas in which it is used. One part of the price is the raw material but another considerable part is the cost of machining components as Ti-alloys are generally considered to be difficult to machine [6, 7]. In practice this means that tools get worn quicker, quality such as surface finish require more work, produced parts needs to be monitored more frequently as tool failure can happen fast, machining speeds needs to be lower and so on, all adding cost to the process. Making the manufacturing more efficient would allow these types of alloys to be used in more applications unlocking potential efficiency gains outside of the specialty areas where they are currently used. Improvements in machining would also help make the process more environmentally friendly with regards to tool consumption as well lowering the overall material footprint of producing Ti-alloy components [8].

The reasons behind the poor machinability are in part connected to the reasons they are used in the first place, e.g. good high temperature strength, as Ti-alloys does not soften much during machining making the process more difficult. The main reason though is often considered to be the poor thermal

conductivity of Ti-alloys which raises the temperature in the tool-workpiece contact zone well above what is seen in steel machining. This increase in temperature leads to a form of chemical wear on the tools by process of diffusion of tool material into the workpiece leading to weakening of the tool and eventual failure [7, 9, 10]. Though this process is well known on a larger scale, the specific details at the atomic level are not. The standard tools used for machining of Ti-alloys are straight grade, uncoated WC/Co tools, examples of which can be seen in figure 1.1. In this work possible wear processes at the atomic scale are investigated to gain a better understanding of how wear progresses, with a focus on the diffusion of C out of the tools and the properties of the interfaces found in the tool-workpiece contact zone.



*Figure 1.1.* WC/Co inserts as used to turn Ti-alloys.

The methods used in this work are all computer based simulation tools, namely Density Functional Theory (DFT), classical Molecular Dynamics (MD) through the use of atomic force fields and kinetic Monte-Carlo (kMC). These methods allow for the study of the atomic scale behaviour of the constituent elements found in the contact zone, but at the expense of restricting the scope to system sizes of a few hundred atoms in the case of DFT to sizes in the region of  $10^4 - 10^5$  atoms in the case of classical MD and  $10^2 - 10^3$  atoms in the case of kMC, all considering how the methods are used in this work, and time scales several orders of magnitude away from anything resembling industrial scales. This places restrictions on the approaches that can be utilized and on the conclusions that can be drawn. In this work a combination of a statistical mechanics approach, through Harmonic Transition State Theory (HTST), a dynamical approach, through classical MD, and kMC is used to study the process of diffusion in experimentally observed WC/W interfaces found in WC/Co tools after turning of Ti-alloys [11, 12]. Further, the properties of WC/W interfaces are investigated using both DFT and classical force fields together with purposely built tools to allow large scale screening of interface parameters. Figure 1.2 shows a graphical summary of the methods used and the work flows followed in this thesis.

This work is divided as follows. First the theory behind the computational methods used is laid out, then a background is given to the phenomena of dif-

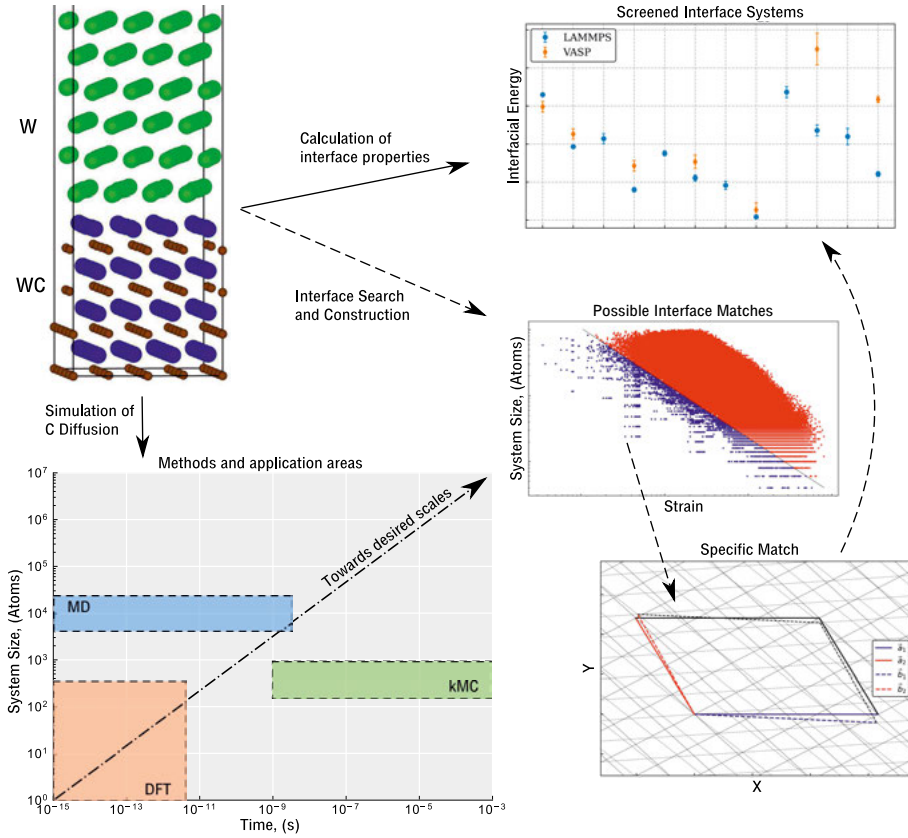


*Figure 1.2.* Methods and work flows, system sizes and timescales reflect how the methods were used in this work.

fusion and the tools which can be used to estimate it as it plays an important roll in this application, then properties of importance relating to surfaces and interfaces are briefly discussed followed by a background to the tool materials and the issues involved in Ti-alloy turning. The main chapters then concern the five papers that this work is built upon. In paper I the diffusion of C in experimentally observed WC/W interfaces is investigated using DFT and HTST and in paper II classical MD is used to investigate the same C diffusion as a function of C depletion. In paper III the construction of a python package to search, build and analyze large sets of interfaces between base structures is described. Which is then used in paper IV to calculate properties of some 60,000 unique interfaces within the WC/W system to determine which are energetically preferred. Finally in paper V the diffusion of C in WC/W interfaces is revisited using kMC.

## 2. Computational Background

In this chapter the underlying theory and justification for the computational approaches utilised in this work is given starting with DFT followed by classical force fields and their applications then the method of MD is presented followed by a description of kMC.

### 2.1 Density Functional Theory

Here, the theoretical background to DFT is presented, with the main body of the theory is built upon [13, 14] with individual references to specific topics. All DFT calculations performed within this work has been made using the Vienna Ab Initio Simulation Package (VASP) [15–17] and the VASP Transition State Tools extension package [18].

#### 2.1.1 Many-Body Description

For calculating the properties of a molecular or solid state system the Shrödinger equation is solved

$$\hat{H}\Psi_i = E_i\Psi_i \quad (2.1)$$

where  $\Psi_i$  is the wave function for the  $i$ 'th state of the system and  $E_i$  the energy of that state.  $\hat{H}$  is the Hamiltonian operator defined as

$$\begin{aligned} \hat{H} = & -\frac{1}{2} \sum_i \frac{\hbar^2}{m_e} \nabla_i^2 + \frac{1}{2} \sum_{i \neq j} \frac{e^2}{|\mathbf{r}_i - \mathbf{r}_j|} - \sum_{i,I} \frac{Z_I e^2}{|\mathbf{r}_i - \mathbf{R}_I|} \\ & - \frac{1}{2} \sum_I \frac{\hbar^2}{M_I} \nabla_I^2 + \frac{1}{2} \sum_{I \neq J} \frac{Z_I Z_J e^2}{|\mathbf{R}_I - \mathbf{R}_J|} \end{aligned} \quad (2.2)$$

where  $i, j$  and  $I, J$  represent indexing for electrons and nuclei respectively,  $e$ ,  $m_e$  and  $\mathbf{r}$  represent the charge, mass and position of the electrons and  $Z$ ,  $M$  and  $\mathbf{R}$  represents the charge, mass and position of the nuclei. The different terms describe the kinetic energy of the electrons, the repulsive electron-electron interaction, the attractive electron-nuclei interaction, the kinetic energy of the nuclei and the repulsive nuclei-nuclei interaction.

## 2.1.2 Born-Oppenheimer Approximation

The first approximation made to equation 2.2 is the Born-Oppenheimer approximation [19] in which the mass of the nuclei are considered infinite in comparison to the mass of the electron, the difference between 1 proton and 1 electron being roughly a factor of 1800, making the fourth term in equation 2.2 negligible, meaning that the kinetic energy of the nuclei are ignored. Further, because of the low mass of the electrons compared to the nuclei they are considered to adjust instantaneously to any change in positions of the nuclei meaning that in principle, from the electron point of view, they will be moving in a stationary potential and the nuclei-nuclei interaction becomes a constant allowing the reworking of equation 2.2 into

$$\hat{H}_e = -\frac{1}{2} \sum_i \frac{\hbar^2}{m_e} \nabla_i^2 + \frac{1}{2} \sum_{i \neq j} \frac{e^2}{|\mathbf{r}_i - \mathbf{r}_j|} - \sum_{i,I} \frac{Z_I e^2}{|\mathbf{r}_i - \mathbf{R}_I|} = \hat{T} + \hat{V}_{ee} + \hat{V}_{ext} \quad (2.3)$$

often termed the electronic Hamiltonian. Where  $\hat{T}$  is the kinetic energy of the electrons,  $\hat{V}_{ee}$  the electron-electron interaction and  $\hat{V}_{ext}$  the fixed potential that the electrons move in which beyond the electron-nuclear interaction may include external potentials, (electronic, magnetic, etc.), applied to the system.

## 2.1.3 Electron Density Approach

DFT is built upon the work of Hohenberg and Kohn [20] and Kohn and Sham [21] which recast the many body problem of interacting particles into a problem involving the particle density and non-interacting particles making the solution of the problem on real scale systems computationally feasible. Hohenberg and Kohn [20] states in two theorems the following as put by *R. M. Martin* in [13].

- **Theorem 1.** For any system of interacting particles in an external potential  $V_{ext}(\mathbf{r})$ , the potential  $V_{ext}(\mathbf{r})$  is determined uniquely, except for a constant, by the ground state particle density  $n_0(\mathbf{r})$ .
- **Theorem 2.** A universal functional for the energy  $E[n]$  in terms of density  $n(\mathbf{r})$  can be defined, valid for any external potential  $V_{ext}(\mathbf{r})$ . For any particular  $V_{ext}(\mathbf{r})$ , the exact ground state energy of the system is the global minimum value of this functional, and the density  $n(\mathbf{r})$  that minimizes the functional is the exact ground state density  $n_0(\mathbf{r})$ .

The consequences of these theorems are that all properties of a system are defined by the ground state electron density. Additionally the energy of the system can be expressed as a functional of the density

$$E_{HK}[n(\mathbf{r})] = T[n(\mathbf{r})] + E_{ee}[n(\mathbf{r})] + \int V_{ext}(\mathbf{r})n(\mathbf{r})d\mathbf{r} + E_{II} \quad (2.4)$$

where  $T[n(\mathbf{r})]$  and  $E_{ee}[n(\mathbf{r})]$  are system independent as they depend only on the electron density and can be collected into the universal  $F_{HK}[n(\mathbf{r})]$  functional and the  $E_{II}$  term represents the constant energy of the nuclei-nuclei interactions. The electron density that minimizes this energy functional is the exact ground state density. The form of the  $F_{HK}[n(\mathbf{r})]$  functional however, is not known.

To get past this, the Kohn-Sham ansatz [21] assumes that the interacting many body system can be substituted for some non-interacting system which gives the same ground state density which can then be solved more easily. The idealised implication of this is that if the correct non-interacting system is chosen then all properties of the original interacting system can be determined. The ground state energy in the Kohn-Sham approach is defined as

$$E_{KS}[n(\mathbf{r})] = T_s[n(\mathbf{r})] + \int V_{ext}(\mathbf{r})n(\mathbf{r})d\mathbf{r} + \frac{1}{2} \iint \frac{n(\mathbf{r})n(\mathbf{r}')}{|\mathbf{r} - \mathbf{r}'|} d\mathbf{r}d\mathbf{r}' + E_{II} + E_{xc}[n(\mathbf{r})] \quad (2.5)$$

where the first term,  $T_s$ , is the kinetic energy of the non-interacting particles, which will differ from the kinetic energy of the interacting particles, however this difference will be incorporated into the  $E_{xc}$  term. The second term is the interaction between the external potential and the electron density the third term is the classic Coulomb interaction within the electron density, termed Hartree energy ( $E_H$ ), the forth term is the constant nuclei-nuclei interaction and the fifth term is the exchange-correlation energy containing all unknown contributions to the total energy. Because of this, apart from approximations to  $E_{xc}$ , the theory is exact. Considering the second Hohenberg-Kohn theorem the ground state particle density of the non-interacting system can be found by minimizing equation 2.5 with respect to  $n(\mathbf{r})$  leading to the Kohn-Sham equations

$$\left( -\frac{\hbar^2}{2m_e} \nabla^2 + V_{KS}(\mathbf{r}) \right) \phi_i(\mathbf{r}) = \varepsilon_i \phi_i(\mathbf{r}) \quad (2.6)$$

where  $\phi_i$  are the Kohn-Sham orbitals,  $\varepsilon_i$  the corresponding energy eigenvalues and  $V_{KS}$  a compact form of the potential terms.

$$V_{KS} = V_{ext} + \frac{\delta E_H}{\delta n(\mathbf{r})} + \frac{\delta E_{xc}}{\delta n(\mathbf{r})} = V_{ext} + V_H + V_{xc} \quad (2.7)$$

The particle density of a system containing  $N$  electrons can then be obtained by

$$n(\mathbf{r}) = \sum_i^N |\phi_i(\mathbf{r})|^2 \quad (2.8)$$

### 2.1.4 Exchange and Correlation Functionals

As stated in the previous section, DFT is exact as long as the precise form of the  $E_{xc}$  functional is known. Unfortunately it is not. Therefore approximations to  $E_{xc}$  must be used, and the design and development of ever better approximations is an active area of research within DFT.

The simplest  $E_{xc}$  functional is the Local Density Approximation (LDA) which was proposed by Kohn and Sham already in [21], it has the form

$$E_{xc}^{LDA}[n(\mathbf{r})] = \int n(\mathbf{r}) \epsilon_{xc}(n(\mathbf{r})) d\mathbf{r} \quad (2.9)$$

where  $\epsilon_{xc}$  is the exchange-correlation energy per particle of a homogeneous electron gas weighted by the particle density at that region. The  $\epsilon_{xc}$  can be divided into the exchange part with the analytical form

$$\epsilon_x[n(\mathbf{r})] = -\frac{3}{4} \sqrt[3]{\frac{3n(\mathbf{r})}{\pi}} \quad (2.10)$$

first derived by Bloch and Dirac [22, 23], and the correlation part,  $\epsilon_c$ , which has no analytical form but has been numerically fitted to simulations e.g. by Ceperly and Alder [24]. Although it may seem like a crude approximation the LDA works remarkably well, however it tends to lead to over binding, i.e. an overestimation of binding energies.

The next level of  $E_{xc}$  functionals are the Generalized Gradient Approximations (GGA), the difference from LDA being that not only the local density but also the gradient of the density at each point is considered. The form of the GGA exchange-correlation functionals are

$$E_{xc}^{GGA}[n(\mathbf{r})] = \int n(\mathbf{r}) \epsilon_x(n(\mathbf{r})) F_{xc}(n(\mathbf{r}), |\nabla n(\mathbf{r})|) d\mathbf{r} \quad (2.11)$$

where  $F_{xc}$  is a dimensionless functional depending on the electron density and its gradient and  $\epsilon_x$  represents the exchange energy per particle of the homogeneous electron gas. Compared to the LDA the GGAs tend to reduce the problem of over binding and GGA functionals created by Becke (B88) [25], Perdew and Wang (PW91) [26] and Perdew, Burke and Enzerhof (PBE) [27] to name a few are used extensively in DFT based research, in this work the PBE functional has been used.

### 2.1.5 Self Consistent Field

Given the theory outlined, culminating in the Kohn-Sham equations 2.6 and armed with an approximate exchange correlation functional, what remains in order to make practical use of DFT is to solve those equations with the specific electron density which yields the global minimum in energy. Since this is not possible in an analytical manner it has to be done self consistently, meaning

that the equation system has to be solved with some initial trial density which is then compared to the resulting density and if self-consistency is not reached within the specified tolerance a new density is generated based on the current acquired density and the procedure is repeated.

### 2.1.6 Basis Sets

In order to solve equation 2.6 the unknown Kohn-Sham orbitals,  $\phi_i$ , needs to be described somehow, preferably in a way that allows equation 2.6 to be solved in a computationally efficient manner. This can be done numerically or as a linear combination of some suitable base

$$\phi_i = \sum_{\mu=1}^N c_{i\mu} \eta_{\mu} \quad (2.12)$$

where  $c_{\mu i}$  are the expansion coefficients and  $\eta_{\mu}$  the chosen basis functions. The accuracy of the description increases as the number of basis functions,  $N$ , increases and at the limit  $N \rightarrow \infty$  the description becomes exact. The choice of basis functions e.g. Gaussian functions or Slater Type Orbitals (STO) for atom centered basis functions or plane waves for non atom centered basis functions, being a combination of computational efficiency considerations, needed accuracy and type of system which is to be described. Using equation 2.12 equation 2.6 can be rewritten as

$$\hat{f}^{KS}(\mathbf{r}) \sum_{\mu=1}^N c_{i\mu} \eta_{\mu} = \epsilon \sum_{\mu=1}^N c_{i\mu} \eta_{\mu} \quad (2.13)$$

where  $\hat{f}^{KS}$  is short hand for the one electron Kohn-Sham operator from equation 2.6. Taking the product with the conjugate of the bases functions and integrating over all space gives us the  $N \times N$  Kohn-Sham matrix on the left hand side of equation 2.13

$$\mathbf{F}_{\mu\nu}^{KS} \int \eta_{\nu}(\mathbf{r}) \hat{f}^{KS} \eta_{\mu}(\mathbf{r}) d\mathbf{r} \quad (2.14)$$

together with the matrix for the expansion coefficients,  $\mathbf{C}$ , and the overlap matrix

$$\mathbf{S}_{\mu\nu} \int \eta_{\nu}(\mathbf{r}) \eta_{\mu}(\mathbf{r}) d\mathbf{r} \quad (2.15)$$

on the right. Transforming the problem to be solved into a system of linear equations

$$\mathbf{F}^{KS} \mathbf{C} = \mathbf{S} \mathbf{C} \epsilon \quad (2.16)$$

solvable by efficient algebraic algorithms.



### 2.1.7 Plane Waves

When modelling crystalline solids it is often convenient to use a plane wave basis set as the system is made up of a lattice which is periodic with respect to the unit cell. This allows the Kohn-Sham orbitals to be expressed as Bloch wave functions

$$\phi_{n\mathbf{k}}(\mathbf{r}) = e^{i\mathbf{k}\cdot\mathbf{r}} u_{n\mathbf{k}}(\mathbf{r}) \quad (2.17)$$

where  $e^{i\mathbf{k}\cdot\mathbf{r}}$  is a plane wave with the periodicity of the unit cell,  $u_{n\mathbf{k}}(\mathbf{r})$  a function with the periodicity of the lattice,  $\mathbf{k}$  a wave vector in the first Brillouin Zone and  $n$  the band index. Further  $u_{n\mathbf{k}}(\mathbf{r})$  can be expanded as a series of plane waves with the periodicity of the lattice which when combined with equation 2.17 leads to

$$\phi_{n\mathbf{k}}(\mathbf{r}) = \sum_m c_{nm}(\mathbf{k}) e^{i(\mathbf{k}+\mathbf{G}_m)\cdot\mathbf{r}} \quad (2.18)$$

where  $c_{nm}(\mathbf{k})$  are the expansion coefficients and  $\mathbf{G}_m$  are discrete reciprocal lattice vectors which obey  $\mathbf{G}_m \cdot \mathbf{R} = 2\pi m$  where  $\mathbf{R}$  is a real lattice vector and  $m$  an integer index. The description of the Kohn-Sham orbitals using plane waves will always contain an error as long as  $m < \infty$ , however this error continuously decreases as a function of the number of plane waves added and in practice an energy cutoff is introduced as

$$E_c = \frac{\hbar^2}{2m_e} |\mathbf{k} + \mathbf{G}_m|^2 \quad (2.19)$$

and only plane waves with energies below  $E_c$  are included in the expansion. When performing calculations using plane wave basis sets one should make sure that total energies are converged to the desired accuracy considering  $E_c$ .

### 2.1.8 Pseudopotentials and Projector Augmented Wave Method

The Kohn-Sham orbitals near the nuclei are characterized by rapid oscillations due to the fact that all orbitals are non-zero close to the nuclei and that the orbitals are required to be orthogonal to each other, away from the nuclei only the valance states are non-zero making the orbitals smoother. These oscillations require a large number of plane waves to be properly described, the effect of which is computationally expensive calculations. Considering that electrons in the shells close to the nuclei contributes less to bonding and chemical reactions than the outer electrons one way around this issue is to combine the potential of the nuclei with the inner shell electrons into one effective potential and additionally separate the wave functions, at a distance  $R_c$  from the core region, into a smooth part below and an unchanged part above with a seamless transition in-between. Commonly used versions of pseudopotentials include norm-conserving pseudopotentials and ultrasoft pseudopotentials [28–30].

The Projector Augmented Wave (PAW) method [31] solves the problem of rapidly oscillating wave functions around the core region by dividing them into two parts, inside and outside some augmentation region  $\Omega$  centered around the nuclei. Unlike the pseudopotential methods the PAW method retains all information of the full wave function inside  $\Omega$ . Outside this region the wave function is unchanged while inside it is described by an auxiliary smooth wave function which is related to the true Kohn-Sham wave function through a linear transformation operator.

### 2.1.9 Forces

To calculate the forces acting on the atoms as a way of relaxing a system or to perform molecular dynamics simulations the Hellmann-Feynman force theorem [32, 33] is used. The force acting on an ion can be described by

$$\mathbf{F}_I = -\frac{\partial E}{\partial \mathbf{R}_I} \quad (2.20)$$

and the total energy of the system is described by

$$E = -\frac{\langle \Psi | \hat{H} | \Psi \rangle}{\langle \Psi | \Psi \rangle} \quad (2.21)$$

considering orthonormality,  $\langle \Psi | \Psi \rangle = 1$ , the force can be described as

$$\mathbf{F}_I = -\langle \Psi | \frac{\partial \hat{H}}{\partial \mathbf{R}_I} | \Psi \rangle - \langle \frac{\partial \Psi}{\partial \mathbf{R}_I} | \hat{H} | \Psi \rangle - \langle \Psi | \hat{H} | \frac{\partial \Psi}{\partial \mathbf{R}_I} \rangle \quad (2.22)$$

where the last two terms will equal 0 as the ground state is a global minimum leading to

$$\mathbf{F}_I = -\langle \Psi | \frac{\partial \hat{H}}{\partial \mathbf{R}_I} | \Psi \rangle \quad (2.23)$$

as the expression for the force.

## 2.2 Classical Force Fields

In this section an overview of classical force field methods will be given as such methods have been used extensively in this work to allow calculations to be performed on systems otherwise computationally unreachable using DFT. All force field calculations in this work have been carried out using the Large-scale Atomic Molecular Massively Parallel Simulator (LAMMPS) software package [34].

### 2.2.1 Concept

The accuracy and transferability of DFT has made it a widely used tool within various scientific fields. However, for all the efficient algorithms and parallel computational ability available today, DFT calculations are still very computationally expensive. VASP, which is used in this work, is a plane wave code scaling as  $N^2 \ln(N)$  or  $N^3$  depending on system size [16] where  $N$  describes the system in terms of electron bands and plane waves, limiting its applicability to system sizes of around a few hundred atoms and timescales in the 10-100 ps range depending on the type of calculation being undertaken. This is in many cases sufficient and other times statistical methods can be used to access properties of interest, but non the less, system size and accessible time scales are perhaps the main limitations of DFT. The limitations arise because of the need to self-consistently calculate the electron density of the studied system in each step. One way around this is to parameterize the expression for atomic interactions, i.e. express the energy of the system as a function of one/several parameters such as interatomic distances, bond angles, etc. At its most basic level this type of calculation scales as  $N^2$  where  $N$  represents the number of atoms in the calculation (compared to electron bands and plane waves in the DFT case), as contributions between each pair of atoms are calculated, but depending on how long range the forces used in the potential are, this can be reduced to a scaling proportional to  $N$  [34], allowing for very fast calculations of the total energy from which other properties can be derived.

As an example equation 2.24 shows the form of the simple, yet sometimes used, Lennard-Jones (LJ) potential [35] parametrized as

$$V_{LJ} = 4\epsilon \left[ \left( \frac{\sigma}{r} \right)^{12} - \left( \frac{\sigma}{r} \right)^6 \right] \quad (2.24)$$

where  $\sigma$  and  $\epsilon$  are parameters which can be tuned to the system of interest and describe the intercept and potential well depth of the binding energy respectively. The increase in computational efficiency between a DFT calculation and a calculation done with a LJ-type potential are many orders of magnitude allowing system sizes of millions of atoms to be simulated in  $\mu$ s timescales. In practice the force fields used are often a lot more sophisticated than the LJ-potential which, aside from certain special cases, lack necessary precision to describe atomic interactions of interest. Commonly used force field types include Embedded Atom Method (EAM), Modified Embedded Atom Method (MEAM), Reax Force Fields (Reax-FF), Morse potentials and Tersoff potentials just to name a few. These potentials often depend on more than just the interatomic distance e.g. taking into account bond angles to nearby atoms, torsion between pairs of neighbouring atoms and being parametrized for multiple atomic species each with individually adapted parametrizations for each of the situations mentioned above, giving them very good accuracy in many cases. This of course slows the calculations down a bit from the LJ-type case

but compared to DFT the speed-up is still many orders of magnitude. There are, unfortunately, many downsides to force field methods as well compared to DFT and an overall summary of the pros and cons are listed below.

- + **Speed.** Depending on the force field used, system sizes of between  $10^4 - 10^7$  atoms can be used to run  $\mu$ s timescale simulations. Interesting benchmark calculations can be found in [36]. This allows for simulations of complex geometries such as interfaces and grain boundaries in general cases which is only possible in special situations using DFT.
- **Transferability.** Compared to DFT where pseudopotentials of atoms  $A$  and  $B$  can be combined to perform calculations on system  $AB$ , force fields are not transferable away from the systems for which they have been optimized.
- **Development.** Optimizations of advanced force fields are very time consuming and, as mentioned in the previous point, only applicable to the specific systems for which they have been optimized. They also require large amounts of experimental/DFT data for fitting and validation. An important step in the usefulness of force field methods in general would be the possibility of fast and reliable on-the-fly generation of force fields leveraging techniques such as machine learning.
- **Predictability.** Since force fields are developed based on empirically fitted models or physical models which, however advanced, still contain large simplifications as compared to the actual systems, it is generally difficult to say anything about the predictive ability of the force fields with regards to parameters for which they have not been fitted. This underlines the importance of evaluating parameters of interest against experiments/DFT when using force fields, however this may not always be possible.

## 2.2.2 Analytical Bond Order Potential

When utilizing force field methods in this work the potential that has been employed is the Analytical Bond Order Potential (ABOP) for the W-C-H system developed by Justlin et al [37] which takes the form of a Tersoff-Brenner-type potential [38–40] with the expressed aim of being able to give good descriptions for all the individual species as well as the binary and ternary mixtures. The atomic interactions in the ABOP are described by the expression

$$E = \sum_{i>j} f_{ij}^c(r_{ij}) \left[ V_{ij}^R(r_{ij}) - \frac{b_{ij} + b_{ji}}{2} V_{ij}^A(r_{ij}) \right] \quad (2.25)$$

where  $i$  and  $j$  represent atomic species,  $f^c$  is a cut-off function described by

$$f^c(r) = \begin{cases} 1, & r \leq R - D \\ \frac{1}{2} - \frac{1}{2} \sin\left(\frac{\pi(r-R)}{2D}\right), & |R - r| < D \\ 0, & r \geq R + D \end{cases} \quad (2.26)$$

which smoothly dampens the potential interactions to 0 over a distance of  $2D$ . The parameters  $V^R$  and  $V^A$  represent the repulsive and attractive contributions to the energy respectively and are described by

$$V^R(r) = \frac{D_0}{S-1} e^{-\beta\sqrt{2S}(r-r_0)} \quad (2.27)$$

$$V^A(r) = \frac{SD_0}{S-1} e^{-\beta\sqrt{2/S}(r-r_0)} \quad (2.28)$$

the  $b_{ij}$  parameter describes the three-body interactions

$$b_{ij} = \frac{1}{\sqrt{1 + \chi_{ij}}} \quad (2.29)$$

with  $\chi_{ij}$  being

$$\chi_{ij} = \sum_{k \neq i, j} f_{ik}^c(r_{ik}) \gamma_{ik} g_{ik}(\theta_{ijk}) e^{\alpha_{ik}(r_{ij}-r_{ik})} \quad (2.30)$$

and finally

$$g_{ik}(\theta_{ijk}) = 1 + \frac{c_{ik}^2}{d_{ik}^2} - \frac{c_{ik}^2}{d_{ik}^2 + (h_{ik}^2 + \cos(\theta_{ijk}))^2} \quad (2.31)$$

all parameters can be found in table 2.1.

**Table 2.1.** *Parameters used in the ABOP potential as developed by [37].*

Parameter	W-W	W-C	C-C
$D_0(\text{eV})$	5.41861	6.64	6.0
$r_0(\text{\AA})$	2.34095	1.90547	1.39
$\beta(\text{\AA}^{-1})$	1.38528	1.80370	2.1
$S$	1.92708	2.96149	1.22
$\gamma$	0.00188227	0.072855	0.00020813
$\alpha(\text{\AA}^{-1})$	0.45876	0.0	0.0
$c$	2.14969	1.10304	330.0
$d$	0.17126	0.33018	3.5
$h$	-0.27780	0.75107	1.0
$R(\text{\AA})$	3.5	2.8	1.85
$D(\text{\AA})$	0.3	0.2	0.15

In the ABOP formalism the energy is parameterized as a function of the interatomic distance between atoms  $i_s$  and  $j_s$  and modified by the distance and angle to atom  $k_s$ , where the subscript signifies the atomic species. In the case of 2 atomic species, e.g. W and C as used in this work, the potential leads to 8 different descriptions, the  $2^3$  permutations of  $s_1s_2s_3$  where  $s$  again signifies the atomic species W or C. The descriptions are then read as follows; Atom 1 is bonded to atom 2 while being influenced by atom 3, figure 2.1 shows a schematic of this for the  $W_1W_2C_3$  and  $C_1W_2W_3$  cases.

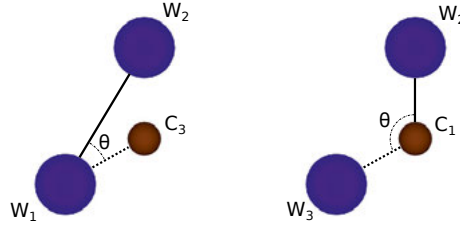


Figure 2.1. Description of naming convention in the ABOP, showing the case of 2 of the 8 possible bonding options in the W-C system. The descriptions correspond to  $W_1W_2C_3$  (left) and  $C_1W_2W_3$  (right).

## 2.3 Molecular Dynamics

In MD a system of atoms, or other particles, is allowed to evolve in time as described by Newton's laws of motion [41]. The forces acting on the species in the system are calculated as

$$\mathbf{f}_i = m_i \frac{\partial^2 \mathbf{r}_i}{\partial t^2} = -\nabla U(\mathbf{r}_i) \quad (2.32)$$

and the system is carried forward a discrete amount in time,  $\delta t$ , based on the forces,  $\mathbf{f}_i$ , where  $i$  signifies individual particles and  $U(\mathbf{r}_i)$  the potential energy of atom  $i$ . Whether the forces are calculated using DFT or from a parameterized expression for the energy determines if the method is to be called Ab-Initio Molecular Dynamics (AIMD) or classical Molecular Dynamics (CMD or simply MD). As the system evolves dynamical properties of interest can be studied. At each point in time the system is described by  $6N$  degrees of freedom, i.e. 3 describing the positions and 3 describing the momentum of each of the  $N$  particles. At any specific time the system is described by these  $6N$  degrees of freedom defining a phase point, the total set of possible phase points is called phase space and the aim of MD simulations is to perform a representative sampling of this phase space which then allows for calculations of properties of interest as time averages over particle trajectories.

When performing MD calculations care has to be taken to ensure that the timestep chosen is short enough to capture the dynamics of the processes that

are being studied, and further, that the system does not drift away from the constant energy hypersurface being sampled. If the above requirements are fulfilled the aim is to explore the systems phase space as efficiently as possible, meaning the use of as large a  $\delta t$  as possible and as few heavy computations as possible, i.e. force evaluations. To achieve this many MD codes use some version of the Verlet algorithm [42] and the codes used in this work mainly use the Velocity-Verlet algorithm [43] which can be defined as

$$\mathbf{p}_i(t + \frac{\delta t}{2}) = \mathbf{p}_i(t) + \frac{\delta t}{2} \mathbf{f}_i(t) \quad (2.33a)$$

$$\mathbf{r}_i(t + \delta t) = \mathbf{r}_i(t) + \frac{\delta t}{m_i} \mathbf{p}_i(t + \frac{\delta t}{2}) \quad (2.33b)$$

$$\mathbf{p}_i(t + \delta t) = \mathbf{p}_i(t + \frac{\delta t}{2}) + \frac{\delta t}{2} \mathbf{f}_i(t + \delta t) \quad (2.33c)$$

where  $\mathbf{p}_i$ ,  $\mathbf{r}_i$  and  $\mathbf{f}_i$  is the momentum, position and force of particle  $i$ .

### 2.3.1 Radial Distribution Function

The Radial Distribution Function (RDF) describes the local environment around a particle or a set of particles and is defined as

$$g(r) = \frac{1}{N} \sum_i^N \frac{N_i(r)}{\rho 4\pi r^2 \Delta r} \quad (2.34)$$

where  $N$  is the number of particles,  $N(r)$  is the number of particles found within the volume of the spherical shells with radii  $r \rightarrow r + \Delta r$  and  $\rho$  is the density. The RDF is useful in determining the ordering of atoms in materials and information about the total number of neighbours at different  $r$  can provide information about the structure of the material.

### 2.3.2 Mean Square Displacement

The Mean Square Displacement (MSD) can be used to calculate the diffusion rate of particles in MD simulations by measuring the square distance traveled as a function of time. It is defined as

$$\langle |r(\tau) - r(0)|^2 \rangle = \frac{1}{NN_t} \sum_{t=0}^{t_m-\tau} \sum_{n=1}^N |r_n(t) - r_n(t + \tau)|^2 \quad (2.35)$$

where  $N$  is the number of particles considered,  $N_t$  the number of timesteps possible when using a timesplit of  $\tau$ , i.e.  $t_m - \tau$ , where  $t_m$  is the total simulation length. In order to get reliable statistics the maximum value for  $\tau$  is usually taken to be significantly less than the total simulation time. In the linear part

of the MSD curve the diffusion rate can be calculated by the Einstein relation which relates the slope of the curve to the diffusion rate as

$$\langle |r(\tau) - r(0)|^2 \rangle = 2dDt + C \quad (2.36)$$

where  $D$  represents the diffusion rate and  $d$  the dimensionality i.e. if the diffusion is measured in 1, 2 or 3 dimensions.

## 2.4 Kinetic Monte Carlo

KMC is a method in which a system is evolved in time not by discrete time steps, as is done in MD simulations, but rather by discrete events. The system is moved from some state  $i$  to some other accessible state  $j$  after which the time for that transition is calculated and the simulation time increased accordingly [44]. This overcomes the problem of simulating processes in systems where events are rare and for that reason it is a popular approach in studying processes such as diffusion. The basic outline is as follows, the probability that the system still resides in state  $i$  at time  $t$  after start is given by

$$p_s(t) = e^{-k_{tot}t} \quad (2.37)$$

where  $k_{tot}$  is the total escape rate given by

$$k_{tot} = \sum_j k_{ij} \quad (2.38)$$

where in turn  $k_{ij}$  are all individual escape rates from state  $i$  by process  $j$ . The probability distribution function,  $p(t)$ , for the time of escape can then be calculated by considering that the integral of  $p(t)$  from  $t = 0$  until some time  $t = t^*$  will equal  $1 - p_s(t^*)$  leading to

$$p(t) = \frac{d}{dt} (1 - e^{-k_{tot}t}) = k_{tot}e^{-k_{tot}t} \quad (2.39)$$

from which the average escape time can be calculated as  $1/k_{tot}$ . The selection of which transition to make is made by ordering the rates of all transitions end to end, considering their relative size, forming a block of size  $k_{tot}$  and drawing a random number in the range  $0 < r \leq 1$ , the process which  $rk_{tot}$  points to is selected as the transition to make. The time is then incremented by drawing an exponentially distributed random number as

$$t_{step} = -\frac{1}{k_{tot}} \ln(r) \quad (2.40)$$

with  $r$  again being a random number in  $0 < r \leq 1$ , whereby the process is started again from the new state. Because the movement from state to state



form a Markov chain [45], i.e. the history of how the system ended up in state  $i$  does not matter, the only properties of importance in each state are the rate constants for the different processes. This loss of memory is related to the separation in timescales between the time spent vibrating within a specific state and the timescale of movement between states.

In order for the above approach to work the rates for the transitions must be known. This can be done by calculating representative transition rates beforehand and building up rate tables which can then be used in every step as the system evolves. But for many systems it is very difficult/impossible to know ahead of time which types of transitions will be possible and many times the actual transitions can be convoluted processes including multiple atoms which will likely not have been known in advance [46]. To get around this Adaptive Kinetic Monte Carlo (AKMC) combines transition state searches with the kMC algorithm to automatically search for transition paths at each state, building up a rate table on the fly and when specified criteria for the completeness of the table is reached a kMC step is taken, rates for previous states are saved for future use and the geometric environment for each transition can be saved to speed up future searches in similar environments. In this work the kMC code EON has been used which, along with many other methods, implements the AKMC approach [47].

### 3. Diffusion, Surfaces and Interfaces

In this chapter the diffusion process will be described as well as the theory and practical methods for evaluating diffusion parameters in simulated systems, the main theoretical framework is built upon [48] with additional references in the text to specific concepts. Additionally, properties of interest for surfaces and interfaces important in this work are covered.

#### 3.1 Atomistic Diffusion

Diffusion on the scale of atoms can be described as the thermal Brownian motion of the atoms. In gases the diffusion can be described by particles moving freely with some mean free path between random collisions with other particles, in liquids it is generally small movements, shorter than the interatomic distances, happening frequently and simultaneously for many particles and in solids it is generally particles sitting in defined sites in the lattice which in random discrete timesteps move between lattice sites, a simplistic though easy to grasp picture of this process can be seen in figure 3.1. Of the three vari-

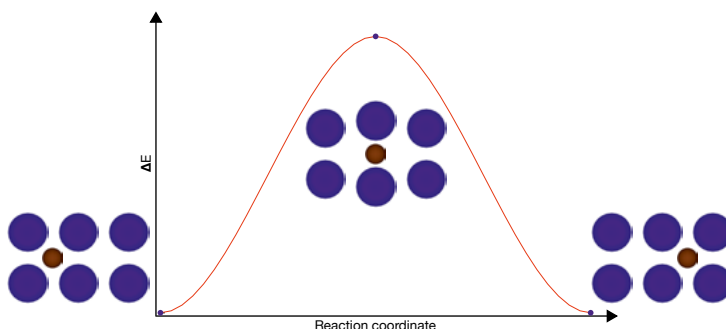


*Figure 3.1.* Schematic description of interstitial diffusion in a lattice, the plot shows the energy barrier  $\Delta E$  as a function of the reaction coordinate.

ants described above the third is by far the slowest, it also has a clear time separation between the time spent in a lattice site and the time moving from one site to the next, in contrast to the continuous movement in the other two cases. In general, atoms residing as interstitials in another lattice move, in the low concentration limit, in a series of uncorrelated jumps as it sees a similar lattice around it at all times, whereas atoms residing as substitutional species in a lattice tend to move with the aid of some diffusion vehicle, i.e. vacancies,

impurities or other defects. Because of this, when a jump has occurred via such a process the mediating vehicle necessarily still resides close by meaning that there is a higher probability for the atom to move back in the direction from once it came leading to some correlation in the jumps which have to be compensated for in those cases. In this work C has been the diffusing species and as such has always been treated as an interstitial.

The rate of diffusion can be described by the Arrhenius expression

$$D = D_0 e^{\frac{-\Delta E}{k_B T}} \quad (3.1)$$

where  $D_0$  is some constant,  $\Delta E$  the activation energy,  $k_B$  Boltzmanns constant and  $T$  the absolute temperature. In the case of a single elementary diffusion step,  $D_0$  can be divided into  $d^2\Gamma$  where  $d$  represents the distance between lattice sites and  $\Gamma$  the frequency with which the atom moves between sites. In a real material the simplest diffusion to describe is uncorrelated interstitial diffusion in an isotropic lattice, in which case the only modification to the above described elementary step is to add the multiplicity of the diffusion path, i.e. multiply the rate by the number of paths available to the interstitial. More advanced models exist to take into account correlated movements and other effects but as the number of different elementary rates grows something like kMC becomes necessary to get the full picture of the diffusion process.

## 3.2 Harmonic Transition State Theory

Through Transition State Theory (TST) one can arrive at the same expression as in equation 3.1 but with a little better understanding of how the different contributions can be calculated [49]. TST sets up a partition function between an initial state  $R$  at some minimum, and a Transition State (TS),  $S$ , separating  $R$  from some product state  $P$ , see figure 3.2. The rate of crossing  $R \rightarrow P$  is then calculated based on the probability of finding the system in the subspace  $S$  given the full space  $R$  and the average flux out of  $S$  in the direction from  $R \rightarrow P$ .

$$k^{TST} = \frac{\int_S e^{-V(\mathbf{x})/k_B T} d\mathbf{x}}{\int_R e^{-V(\mathbf{x})/k_B T} d\mathbf{x}} \langle v_{\perp} \rangle = \frac{Z_S}{Z_R} \sqrt{\frac{k_B T}{2\pi m}} \quad (3.2)$$

To estimate the partition function in equation 3.2 the potential energy contribution  $e^{-V(\mathbf{x})}$  can be expanded in a Taylor series leading to the equation

$$k^{HTST} = \frac{\prod_{i=1}^{3N} \nu_{R,i}}{\prod_{i=1}^{3N-1} \nu_{TS,i}} e^{\frac{-(V_{TS}-V_R)}{k_B T}} = \tilde{\nu} e^{\frac{-\Delta E}{k_B T}} \quad (3.3)$$

which defines Harmonic Transition State Theory (HTST). Where  $\nu$  are the vibrational frequencies at the minimum and the TS respectively, defined together

with the harmonic spring constant  $k$  from the Taylor expansion as

$$v = \frac{1}{2\pi} \sqrt{\frac{k}{m}} \quad (3.4)$$

and the  $3N$  and  $3N - 1$  products represents the dimensionality of  $R$  and  $S$ . One consideration when using TST in general is that in order for the assumption of a Boltzmann distribution in the initial state to be valid the barrier should be larger than  $5k_B T$ .

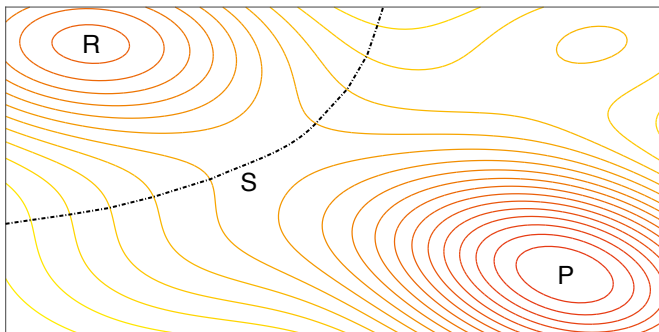


*Figure 3.2.* Schematic image of a potential energy surface with a reactant state, R, a transition state, S, and a product state, P.

### 3.3 Nudge Elastic Band

Nudge Elastic Band (NEB) is a method for finding TS, i.e. saddle points, on a Potential Energy Surface (PES) between two known endpoints [50, 51]. This is done by placing a string of images, normally linear interpolations, from the initial state to the final state then connecting these images by a force acting as a spring between each image connecting each with its neighbors. The images are then allowed to relax while under the influence of the spring force and the true force component perpendicular to the tangent between each of the images and their higher energy neighbor driving the system towards the Minimum Energy Path (MEP), i.e. the likely reaction pathway from the initial state through the TS to the final state, a schematic image of this process can be seen in figure 3.3. The energy difference between the starting state and the TS represents the activation energy or diffusion barrier seen as  $\Delta E$  in equation 3.1 and 3.3. This method will, disregarding convergence issues, find a pathway from the starting state to the final state but since the initial rough pathway have been predetermined at the moment of placing the images there is no guarantee that it will find the true MEP of the system and as such should always be a consideration when evaluating the results. An Extension to the NEB method is the Climbing

Image NEB (CI-NEB) in which the highest energy image is cut loose from the spring force and the true force component acting in the direction of the spring force is inverted causing the image to climb the PES towards the saddle point [52]. All NEB calculations in this work have been performed with the VASP extension code VTST [18].

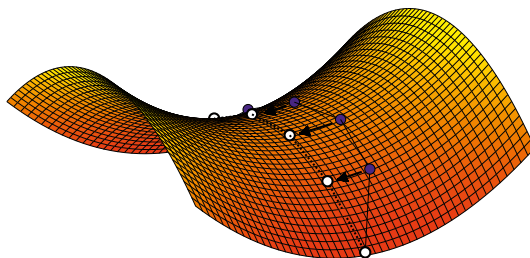


Figure 3.3. Schematic description of the NEB process, blue dots are initial linear estimates for the MEP, the white dots represents the relaxed MEP crossing the TS.

### 3.4 Dimer

The dimer method is, similar to the NEB, a method for finding TS on a PES but beyond that the methods are quite different [53]. In the case of the dimer method the system is split up into two different *images* or *replicas* (the concept of the two replicas giving the method the name dimer), each described by the  $3N$  coordinates of the atoms that make up the two systems, separated by some small distance from their common midpoint. The method then consists of evaluating the energy and the force acting on the two different replicas and using that information to guide the center of the dimer towards the TS. The convergence towards the TS is done in two steps. First the dimer is rotated around its center point based on the forces acting on the replicas, where an expression for the rotation angle needed to minimize the dimer energy and align it in the direction of the lowest curvature mode can be found by Taylor expanding the potential energy around the midpoint. Secondly, after the dimer has been aligned in the direction of the lowest curvature mode the dimer is translated by the forces acting on the center of the dimer. Since those forces will act to move the dimer down the PES away from the saddle point the component of the force parallel to the dimer is inverted leading to the convergence of the dimer towards the TS which is a maximum along the lowest curvature mode of the PES. One additional modification to this which is introduced is to treat regions where the minimum curvature mode is convex, i.e. regions close to potential energy minimas, differently from regions where at least one curvature is concave in order to speed up convergence. The modification is simply that in all-convex regions the force is taken to be the inverted force acting par-

allel to the dimer causing the dimer to quickly climb out of the convex region instead of only inverting the force component along the dimer. Other methods for finding saddle points include e.g. the Activation Relaxation Technique (ART) [54].

Below is a short summary of the strengths and useful situations for the NEB and the dimer method respectively.

- **Reaction path (NEB).** If the energy along the reaction path between two states is of interest than the NEB method provides that information whereas the dimer does not.
- **Simple paths (NEB).** It may be hard to know beforehand, but in systems with clearly defined diffusion paths the NEB method is simple and straight forward to use and together with the climbing image only a single image will be needed to find the TS.
- **Unknown paths (Dimer).** In systems without clear diffusion paths the dimer method provides a means of searching different pathways without discrimination enabling unknown diffusion mechanisms to be found.
- **Cost (Dimer).** Since the dimer method only uses 2 replicas of the system the computational cost compared to a multi image NEB calculation is much lower.
- **Scripting (Dimer).** Since the dimer method allows the dimer to be placed at any point on the PES and pointed in a random initial direction whereby it will start to work its way towards the TS, the method is excellent as a building block in automated TS search codes.

## 3.5 Surfaces

Surfaces and interfaces are important for material properties in many applications ranging from electronic properties in 2D materials to structural properties in bulk materials. Both surfaces and interfaces can be considered as deviations from otherwise periodic bulk structures and described by associated energy contributions. For surfaces the main property of interest is the surface energy representing the added energy cost of the surface as compared to a continuous bulk structure and can in the simplest case be calculated as

$$\sigma = \frac{E_S - E_B}{2A} \quad (3.5)$$

with  $E_S$  and  $E_B$  being the total energy of the surface slab and the equivalent amount of bulk respectively and  $A$  the surface area.

Depending on the structure and the type of surface of interest the above approach is not always possible since the construction of the surface slabs might lead to different terminations of the top and bottom surfaces. For WC specifi-

cally, which is the main focus in this work, the surfaces are mainly terminated by the basal and prismatic planes [55, 56], see figure 3.4, and constructing surface slabs of either leads to different terminations of the two surfaces. For the basal terminations one surface will be W terminated while the other will be C terminated if the stoichiometry is to be kept. The standard way of dealing

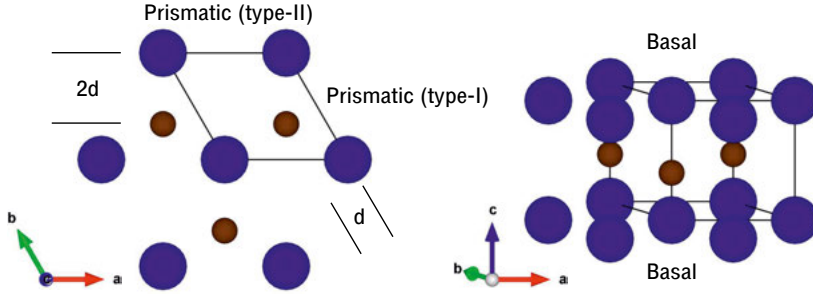


Figure 3.4. Cells showing the prismatic (left) and basal (right) terminations of WC.

with this is to construct a range for the chemical potential [57–59] of either W or C and have it be bound by the formation enthalpy of the appropriate phases, here WC and graphite, leading to

$$\Delta H_f^{WC} \leq \mu_C - \mu_C^B \leq 0 \quad (3.6)$$

with  $\mu_C$  and  $\mu_C^B$  being the chemical potential of C to be selected and the chemical potential of C in its bulk form and  $\Delta H_f^{WC}$  the formation enthalpy of WC calculated as

$$\Delta H_f^{WC} = \mu_{WC}^B - (\mu_W^B + \mu_C^B) \quad (3.7)$$

with  $\mu_i^B$  being the chemical potential of each respective bulk configuration. After selecting a value for the chemical potential within the specified range from equation 3.6 the surface energy of the basal termination of the stoichiometric WC can then be calculated as

$$\sigma = \frac{E_S - N_W \mu_{WC}^B + (N_W - N_C) \mu_C}{2A} \quad (3.8)$$

by using elementary symmetrically terminated slabs with  $N_i$  representing the number of atoms of W and C used in the slabs and the rest as previously defined.

In addition to the basal planes the prismatic planes are of interest as well and in addition to the issue of stoichiometry described above the task is made difficult by the fact that the prismatic surfaces differ in the geometric structure of the terminations as well. Looking at figure 3.4 the prismatic terminations come in two variations, often termed type-I and type-II [60], with the difference being the final inter-planar distance which is  $d$  for the type-I termination and  $2d$  for the type-II termination. Several different ways exist for calculating

the surface energies for these surfaces but in this work the approach taken is the one described in [37] where the ratio between the C and W terminations for the two types of prismatic surfaces are considered to be equal from which the individual contributions can then be calculated.

### 3.6 Interfaces

Surfaces and interfaces are intimately connected for obvious reasons as any interface is made up of individual surfaces. The main interface parameters of interest in this work is the work of adhesion and the interfacial energy. Where the work of adhesion describes the energy needed to separate an interface into its individual surface slabs providing a value for the stability of the interface in relation to the free surfaces. It can be calculated as follows

$$W_{ad} = \frac{E_{S1} + E_{S2} - E_I}{A} \quad (3.9)$$

where  $E_{S1}$ ,  $E_{S2}$  and  $E_I$  represent the total energy of the two individual surfaces and the interface respectively with  $A$  being the area of the interface. The work of adhesion can be used to compare the stability of different interfaces constructed from the same initial surface slabs to find which are energetically favorable.

The interfacial energy represents the excess energy needed to create an interface from the equivalent bulk structures and can be calculated either as the energy difference between the interface and the respective bulk structures or from the work of adhesion and the surface energies as

$$\gamma = \sigma_{12} + \sigma_{21} - W_{ad} \quad (3.10)$$

where  $\sigma$  represents the surface energies of the surfaces that make up the interface and  $W_{ad}$  the work of adhesion [58, 60]. The interfacial energy allows for the comparison of interface stability between interfaces built from different initial surfaces allowing conclusions to be drawn as to which interfaces are likely to be most common in a given material system.



## 4. Cemented Carbides in Metal Machining

In this section an overview is given to the material system studied in this work, cemented carbides, or specifically tungsten carbide with a cobalt binder phase (WC/Co). Details behind its application as it applies to machining of Ti-alloys will be covered together with a brief overview of the properties of different Ti-alloys and associated issues of interest to this work.

### 4.1 Cemented Carbides

Cemented Carbides (CC), or hard metals as they are sometimes called, are a group of composites which consists of hard carbides/nitrides in a ductile metal matrix providing a combination of hardness through the carbides as well as toughness through the metal matrix. In the first marketed product WC were combined in a Co matrix by the German company Friedrich Krupp, which is still, with additional inclusions, the main composition present in more than 80% of all CCs, but now other compositions in the same family exist as well where the structure of the CC is more application specific and tailored with respect to grain size and shape, inclusion of cubic carbides, e.g. TiC, TiN ( $\gamma$ -phase), composition gradients, particle reinforcement to name a few. WC/Co is used extensively as wear parts and in heavy duty drilling and boring within mining, oil extraction and excavation and in wood working industries and, as is studied in this work, within metal cutting [61].

Considering the WC grains in particular, the standard grain sizes in metal machining are between 0.5-2  $\mu\text{m}$  with a Co content of 5-15%. WC is a stoichiometric compound with virtually no deviation from its W/C ratio of 1, it has a hexagonal structure and below 1520 K any C deficiency or surplus leads to the formation of BCC W or graphite respectively. Figure 4.1 shows the phase diagram for the W-C system calculated in Thermo-Calc [62]. The relevant temperatures for this work, i.e. the temperatures that have been reported for the tool/workpiece contact during Ti-alloy turning, are in the range of 1073-1373 K [1, 9, 10] but at slightly higher temperatures, starting at 1520 K, the  $\text{W}_2\text{C}$  phase starts to become stable which may be of interest as exact temperatures in the cutting zone are unavailable.

### 4.2 Ti-Alloys

The main reasons for using Ti and Ti-alloys are their high strength to weight ratio, good high temperature strength and chemical inertness including corro-

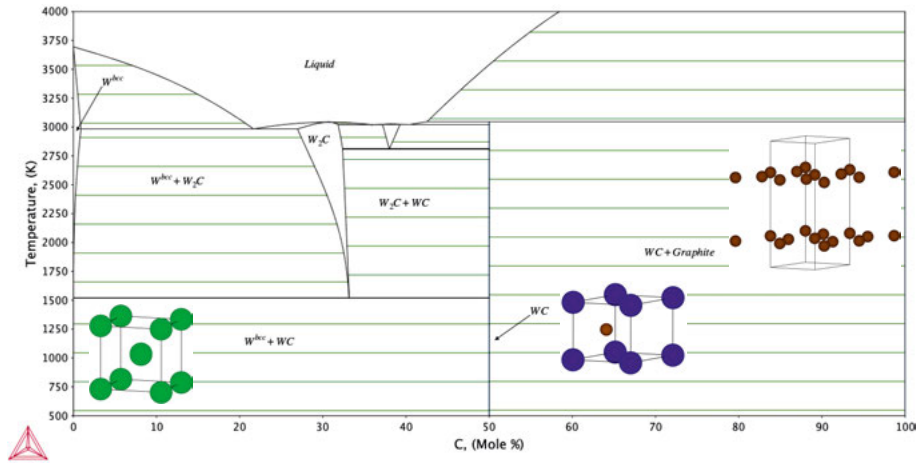


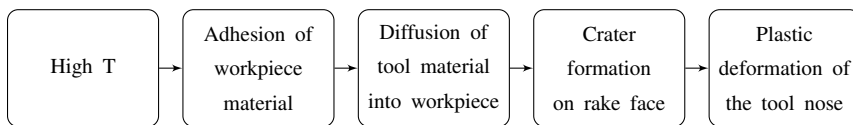
Figure 4.1. Phase diagram of the W-C system at a pressure of 1 bar along with the unit cells for the most relevant structures (in this work) BCC W (left), WC (middle) and graphite (right).

sion resistance [3, 4]. Based on their composition Ti-alloys can be divided into 4 groups,  $\alpha$ -, near  $\alpha$ -,  $\alpha/\beta$ - and  $\beta$ -alloys where  $\alpha$  is the low temperature phase which has an HCP structure and is stable up to 1155 K while  $\beta$  is the high temperature phase which has a BCC structure. Below is a short summary of the different groups [1, 2, 4, 63].

- $\alpha$ . Pure Ti and alloys containing O and Fe, mainly used in high corrosive environments in low temperatures.
- Near  $\alpha$ . Alloys containing mostly  $\alpha$ -phase alloyed with  $\alpha$ -stabilizing elements, Al, Sn and Zr and small amounts of  $\beta$ -phase with  $\beta$ -stabilizers, Mo, V, Nb. Mainly used in applications in the temperature range 670-800 K, examples include Ti-6Al-5Zr-0.5Mo-0.25Si (IMI-685).
- $\alpha/\beta$ . Alloys with a mixture of  $\alpha$ - and  $\beta$ -phase. Used in structural applications and showing good resistance to corrosion, this group contains the common alloy Ti-6Al-4V (Ti-64 or IMI-318) which account for roughly 60% of the total alloy production and which have been used in the experiments whose observations are taken as the starting point for what is studied in this work.
- $\beta$ . Alloys with high amounts of  $\beta$ -stabilising elements showing high strength and good hardenability and good resistance to stress corrosion, examples include Ti-10V-2Fe-3Al (Ti-10-2-3).

### 4.3 Ti-Alloy Machining

Ti and Ti-alloys are generally considered difficult to machine, meaning that tools get worn quicker, machining speed needs to be lower and the quality control of the final product needs to be more rigorous and tools need to be changed frequently [6, 7]. The reasons for this have some overlap with the reasons that Ti-alloys are used in the first place, e.g. good high temperature strength. When machining steels they tend to soften considerably in comparison to the CC tools used to machine them during operations but this is not the case for Ti-alloys [2]. Further, Ti is very reactive with the tool elements, (W, C and Co), at the elevated temperatures in the contact zone [9]. Focusing specifically on turning the standard approach is to use straight grade uncoated WC/Co tools. Coatings which very successfully extend the tool life in many other metal working applications can in fact degrade tool life in Ti turning, explained as due to the preferential dissolution of coating material (O, N, C, B) in the Ti [10]. Finally, and most importantly, the poor thermal conductivity of Ti-alloys, being around 7 W/mK (Ti-64) compared to around 50 W/mK for carbon steel leading roughly 80% of the heat generated in the turning operation to dissipate away through the tool compared to only 50% in steel turning [1]. This raises the cutting zone temperature well above what is seen in steel turning, with estimates ranging from 1073-1373 K [1, 9, 10], this elevated temperature leads to diffusion playing a major part in the wear of the tools. Several investigations have been made based on experiments, diffusion couples and simulations to better understand the wear behaviour and how it progresses during Ti-alloy turning [7, 9–12, 64–68], differences can be seen between different types of alloys but the main conclusions are some combination of dissolution/diffusion of tool material in the workpiece with the wear progression described as follows.



The picture of diffusion as the main reason behind the tool wear is well illustrated in figure 4.2 where the smoothly worn crater after turning operations is visible which is a sign of a large chemical component to the wear, adhesion of workpiece material can be seen as well, both on the edge and in the crater region.

Investigations into worn tools after turning of Ti-64 have showed that a thin layer, about 100 nm, of BCC W exists on top of the outermost WC grains [11, 12]. This was observed by Scanning Electron Microscopy (SEM), Energy Dispersive Spectroscopy (EDS) and X-Ray Diffraction (XRD). A Transmission Electron Microscopy (TEM) image of such a layer can be seen in figure

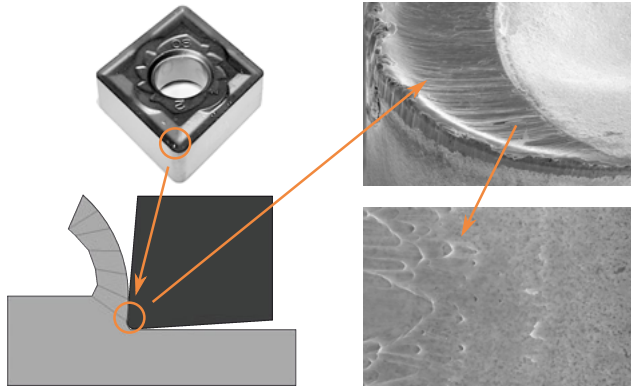


*Figure 4.2.* Images showing the WC/Co insert (top left), a schematic of the turning process (lower left), the smooth crater on the insert (top right) and adhered Ti from the crater (lower right), SEM images courtesy of Martina Lattemann and Sandvik Coromant.

4.3. Since W is only present in the contact zone in the form of tool material the only way a pure W layer can form is through removal of C and the rate of C removal is one piece of the puzzle in formulating a theory for how wear progresses in WC/Co materials during turning of Ti-alloys and for that reason it is the main focus of this work.

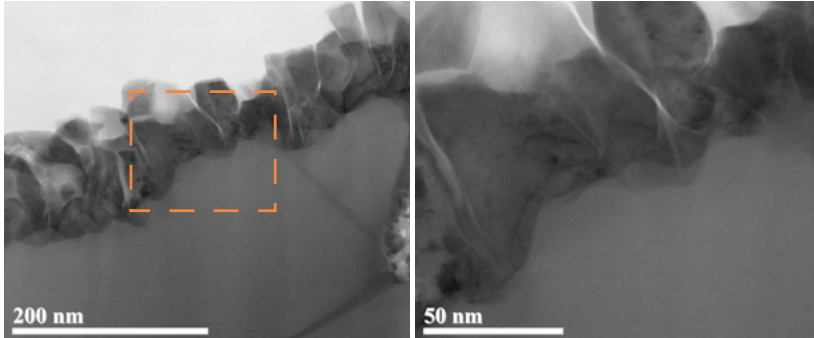


*Figure 4.3.* TEM images of WC grains with a C depleted layer on top, the area indicated in the left image is the same part which is shown in the image to the right, image courtesy of Martina Lattemann and Sandvik Coromant.

## 5. DFT Study of C Diffusion in WC/W Interfaces

In paper I the WC/W interfaces that exist as a consequence of the C depletion of the WC structure, examples of which can be seen in figure 4.3, were investigated. The background for this being that a well defined BCC W layer ontop of the WC grains must mean some equilibrium between its creation and removal. There are some different ways to remove the BCC W, abrasive removal once it gets large enough or dissolution in the workpiece material as W starts to form a solid solution with Ti at temperatures above 1150 K. Whereas the only way to create this layer is to remove C from the WC grains, for this reason the rate of C diffusion out of the WC and into the WC/W interface is of interest. The results show a 3.3 eV diffusion barrier for the movement of C through the final layer of a basal terminated WC surface in contact with BCC W and a 1.5 eV diffusion barrier for the movement through a prismatic terminated WC surface. Within the interfaces the barriers are largely similar between the two types of WC terminations varying roughly between 0.8-1.5 eV.

### 5.1 Computational Approach

The model interfaces used were selected based on the approach of minimizing the mismatch strain between the individual base cells using the method described in [69] and implemented in the VNL software package [70]. In addition to minimizing the strain in the interfaces the size was considered as well in order to make the interfaces computationally manageable. Finally, the shape of the interfaces were considered as the periodic boundary conditions mean that a narrow interface in any one direction leads to interactions between diffusing atoms in neighbouring cells. The interface search was set up by matching a prismatic type-I W terminated WC cell and a basal W terminated WC cell against the low index terminations of BCC W with the WC unstrained as the bottom surfaces and the BCC W strained as the top surfaces. The selected interfaces were  $[10\bar{1}0]/[100]$  and  $[0001]/[111]$ , properties of which can be found in table 5.1 and shown in figure 5.1.

All DFT calculations were carried out using VASP [15–17] and the extension code VTST [18]. In the calculations the bottom two layers of the WC were frozen as to enforce bulk WC atomic distances and to have a stable base

**Table 5.1.** *Interfaces used in paper I*

WC/W	Length a/b (Å)	Angle a/b	Strain a/b (%)	Atoms
[0001]/[111]	13.38/ 7.72	90°	-0.58/-0.58	178
[10 $\bar{1}$ 0]/[100]	11.68/11.38	90°	2.12/-0.59	251

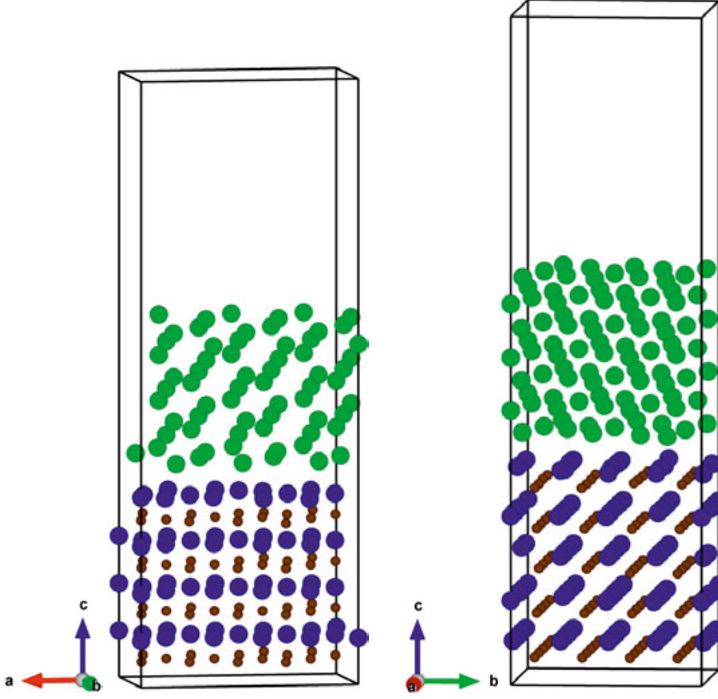


Figure 5.1. Cells showing the basal interface (left) and the prismatic interface (right). Blue atoms are W in WC, brown atoms are C and green atoms are W in bcc W.

for the diffusion calculations. A combination of the NEB and dimer methods were then used to map out the elementary diffusion steps for C atoms moving first out of the WC into the WC/W interfaces and then within the interfaces. For the movement of C atoms into the interfaces the NEB method was used as the diffusion path through the last layer of W in the WC is well defined for both interfaces. After finding the relevant saddle points HTST were used to estimate the attempt frequencies and construct the diffusion rates.

Once the initial barriers and attempt frequencies for C moving into the interfaces were found the dimer method was used to map out diffusion paths within the interfaces. The reason for switching to the dimer method was that unlike the initial diffusion step the diffusion within the interfaces have no obvious paths and using the NEB method would force estimates of the paths to be chosen beforehand. Using the dimer instead allows for unbiased searches for transition states after which relaxations can be made to find the connected

energy minima. Once the transition states were found HTST were used in the same way as before to calculate the attempt frequencies and arrive at the diffusion rates. The full set of discovered diffusion paths for both interfaces can be seen in figures 5.2 and 5.3.

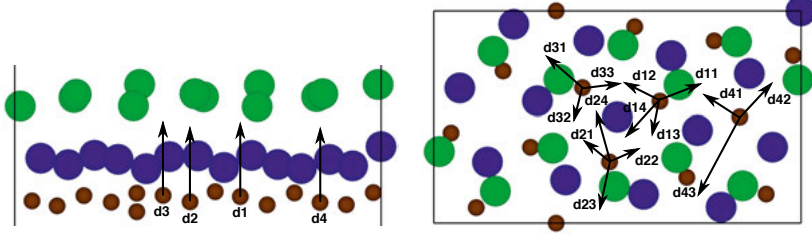


Figure 5.2. The investigated diffusion directions for the basal interface.

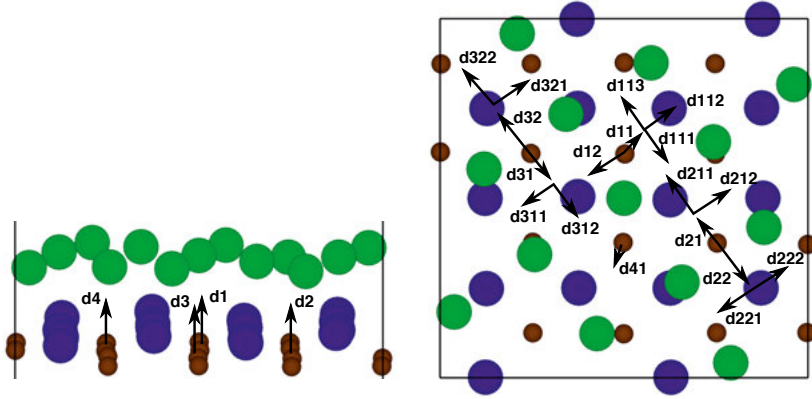


Figure 5.3. The investigated diffusion directions for the prismatic interface.

In addition to the diffusion paths investigations were also made to check if it would be energetically favorable for the C atoms to move into the BCC W or to reside close to the interface. This was done by relaxing the diffusing C atom in octahedral sites at increasing distances away from the interface and comparing the total energy as a function of distance.

## 5.2 Results and Discussion

The diffusion barriers for the movement of C into the interfaces show consistent values in all cases when considering the symmetry of the paths. For the basal terminated WC the barriers for the d1, d2 and d3 directions as marked in figure 5.2 are all around 3.3 eV which is very high and slightly more than twice as high as the diffusion barriers in the prismatic interface which are all 1.5 eV. The high values in both cases show that both terminations are expected

to be very stable and rule out the possibility of studying the initial diffusion of C out of the WC by means of AIMD at a reasonable computational cost. The difference between the two interfaces mirror the values seen for the diffusion barriers in bulk WC as well. If studied using equivalent computational parameters in a  $3 \times 3 \times 3$  unit cell of WC with a C vacancy to mediate the diffusion the barriers for moving through the basal and the prismatic planes are around 6.3 and 3.4 eV respectively, i.e. roughly twice the values seen for moving through the truncated bulk represented in the interfaces. With the large difference seen between the two WC surfaces it would be expected to see some directional preference in the wear unless some other process counteracts this.

For the diffusion within the interfaces the same consistency in the diffusion barriers between equivalent directions is found. Further, the differences seen between the basal and prismatic interfaces are largely gone once the C is in the interface. Dividing the diffusion steps into groups based on the paths taken shows this clearly, see figure 5.4.

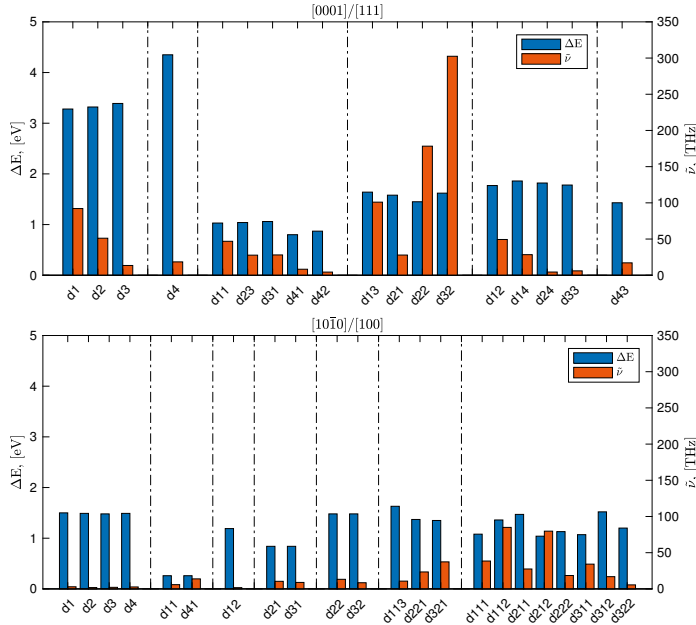


Figure 5.4. Activation energy (blue) and attempt frequency (red) for the basal interface (top) and the prismatic interface (bottom).

In the basal interface the diffusion paths are all in one layer directly within the interface whereas for the prismatic interface the diffusion paths are separated into two layers. The first being in the middle of the interface while the second being in the bottom layer of the BCC W. Both types of diffusion paths in the prismatic interface follow the cell vectors of the original BCC W and within the bottom layer the movement occurs between what would be octahe-



dral sites in full BCC W, depending on the local environment at each step the C atoms either falls down into the middle of the interface or stay in the bottom BCC W layer.

For the attempt frequencies the variation is larger than what is seen for the diffusion barriers but most lie between 1-100 THz with somewhat higher values for the basal interface. For the prismatic interface differences can be seen between the different diffusion regions as well, i.e. the movement into the interface the movement from the interface to the bottom BCC W layer and the movement within that layer, the same trends are not as clear for the basal interface. The full estimates of the elementary diffusion rates for the different groups of identified diffusion directions can be seen in table 5.2

**Table 5.2.** *Mean activation energies and pre-factors along with the standard error for the different groups of identified directions.*

WC/W	Group	$\Delta E$ , (eV)	$D_0$ , ( $m^2/s$ )
[10 $\bar{1}$ 0]/[100]	d1, d2	1.49(0)	6.4(7)E-8
	d3, d4		
[10 $\bar{1}$ 0]/[100]	d11, d41	0.26(0)	2.2(9)E-7
[10 $\bar{1}$ 0]/[100]	d12	1.19(0)	1.3(0)E-7
[10 $\bar{1}$ 0]/[100]	d21, d31	1.48(0)	3.2(7)E-7
[10 $\bar{1}$ 0]/[100]	d22, d32	0.84(0)	2.2(2)E-7
[10 $\bar{1}$ 0]/[100]	d113, d221	1.45(9)	6.4(21)E-7
	d321		
[10 $\bar{1}$ 0]/[100]	d111, d112	1.23(7)	9.4(36)E-7
	d211, d212		
	d222, d311		
	d312, d322		
[0001]/[111]	d1, d2	3.33(3)	3.9(17)E-6
	d3		
[0001]/[111]	d4	4.35(0)	1.9(0)E-6
[0001]/[111]	d11, d23	0.96(5)	9.8(31)E-7
	d31, d41		
[0001]/[111]	d42	1.57(4)	3.2(14)E-6
	d13, d21		
[0001]/[111]	d22, d32	1.80(2)	1.5(7)E-6
	d12, d14		
[0001]/[111]	d24, d33	1.43(0)	2.6(0)E-6
	d43		

Finally, the results from the energetic preference for where the C diffusion would occur show that the preferred location for the diffusion is at or within the interface as the energy increases away from the interface as can be observed in figure 5.5 reflecting the high chemical potential of C in BCC W.

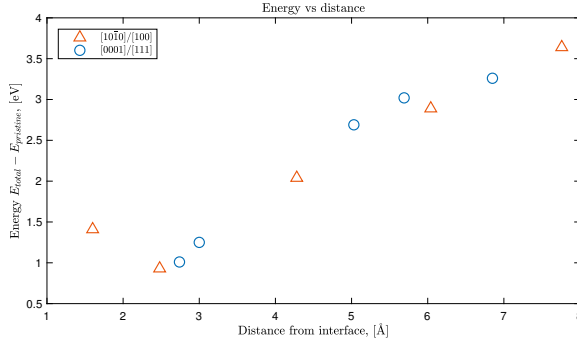


*Figure 5.5.* Energy for a C interstitial relaxed in octahedral sites at increasing distance from the interface for the basal interface (blue circles) and the prismatic interface (red triangles)

The results presented here, though fairly large scale, only provides information on the elementary steps present in these interfaces. For a full picture of the diffusion occurring in these interfaces something like kMC needs to be used, something which is done in paper V.

## 6. MD Simulations of C Diffusion as a Function of C Depletion

In paper II the evolution of C diffusion in WC/W interfaces were studied as a function of temperature and C depletion in the outermost layer of WC. Though the barriers found for the initial diffusion steps are much too high to reasonably expect to see a relevant number of diffusion events occurring using MD on pristine interfaces this turns out to be clearly different when the outermost layer becomes depleted of C. Here, 5 different C depletion percentages and 9 different temperatures in the range from 673-1873 K were investigated and the results show a clear increase in C mobility with both temperature and C depletion. At low depletions the interfaces show similar stability to the pristine interfaces at all temperatures while at higher depletions only the lowest temperatures are stable. Once the C starts to move both the basal and prismatic interfaces show similar results which might explain why clear directional preferences are not seen in the worn tools.

### 6.1 Computational Approach

Similar to paper I interfaces were built using the method described in [69]. As a classical potential was used, the ABOP for the W-C-H system developed by [37], the limitations on system size that were critical in paper I could be overcome. Here, the selected low strain interfaces were scaled up to contain at least 20,000 atoms in order to get better statistics for the diffusing C atoms. In total 6 different interface combinations were built, a basal W termination and a prismatic W type-I termination of WC paired against each of the low index terminations of BCC W, all of which are described in table 6.1. All simulations in this paper were carried out using LAMMPS [34].

The approach taken to investigate the C diffusion in this paper was different from the approach in paper I in that it used MD and the calculation of the MSD for the C atoms as described in section 2.3.2. Initially in order to benchmark the ABOP to the DFT results NEB calculations were done to compare the diffusion barriers for the movement of C into the interfaces. The results showed barriers of 1.9 (1.5) and 2.9 (3.3) eV respectively for the prismatic and basal interfaces with the value in parenthesis being the DFT values as calculated in paper I. Though the difference is significant for the prismatic termination the differentiation between the two types remain and the results for the basal

**Table 6.1.** *Interfaces used in paper II.*

WC/W	Length a/b (Å)	Angle a/b	Strain a/b (%)	Atoms
[0001]/[100]	70.7/99.2	90°	-0.06/0.09	33,292
[0001]/[110]	58.3/76.5	80.1°	-0.02/0.01	20,576
[0001]/[111]	86.3/74.8	90.0°	-0.00/0.00	29,184
[10 $\bar{1}$ 0]/[100]	96.4/58.9	103.0°	0.00/-0.02	22,986
[10 $\bar{1}$ 0]/[110]	68.4/77.7	77.3°	0.00/-0.02	22,056
[10 $\bar{1}$ 0]/[111]	101.7/70.4	74.8°	0.01/0.00	28,030

termination agrees fairly well and as such results were deemed to be relevant though in a slightly more qualitative sense for the prismatic terminations.

As the interesting points of study were the diffusion rates as a function of C depletion and as a function of temperature calculations were performed for random C depletions of 10%, 30%, 50%, 70% and 80% and at temperatures of 673 K, 873 K, 973 K, 1073 K, 1173 K, 1273 K, 1373 K, 1573 K and 1873 K. Further, as the results are determined by the initial random deletions and the initial random velocities each simulation were run 4 times using different random seeds for those properties. The timescales simulated were 500 ps in 3 runs and 2500 ps in 1 run all using a timestep of 1 fs. The preparation for each interface calculation were done by initial equilibration using an NPT ensemble for 25 ps to reduce the pressure in the interface cells to 0 followed by an NVT ensemble for 25 ps before the main calculation began, again, using an NVT ensemble together with a Nose-Hoover thermostat [71, 72]. In each step the bottom layers in all interfaces were frozen and the temperature and pressure were controlled by the mobile atoms and in the case of the NPT equilibration the static atoms were scaled along with the cells in the x and y directions parallel to the interfaces.

From the MSD trajectories at different temperatures the contributions to the diffusion rate in the form of the energy barrier and the pre-factor were quantified by fitting the data as

$$\ln(D) = \ln(D_0) - \frac{\Delta E}{k_B T} \quad (6.1)$$

with  $D$  being the diffusion rate,  $D_0$  the pre-factor,  $\Delta E$  the diffusion barrier,  $k_B$  boltzmanns constant and  $T$  the temperature. The fit was broken up into two parts, above and below 1520 K as that is where  $W_2C$  becomes stable, this is well above any reported cutting zone temperature but was included to complete the picture outside the immediate frame of the studied application.

## 6.2 Results and Discussion

The results for all simulations together with the fits according to equation 6.1 are shown in figure 6.1. As can be seen the diffusion rates increase as both

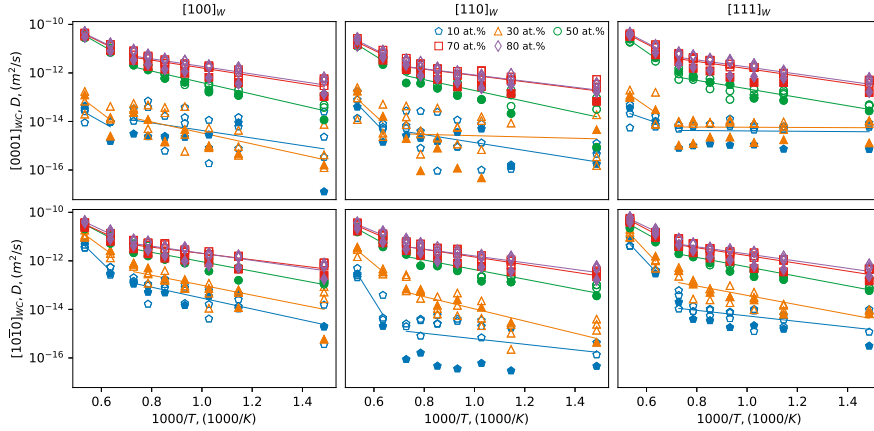
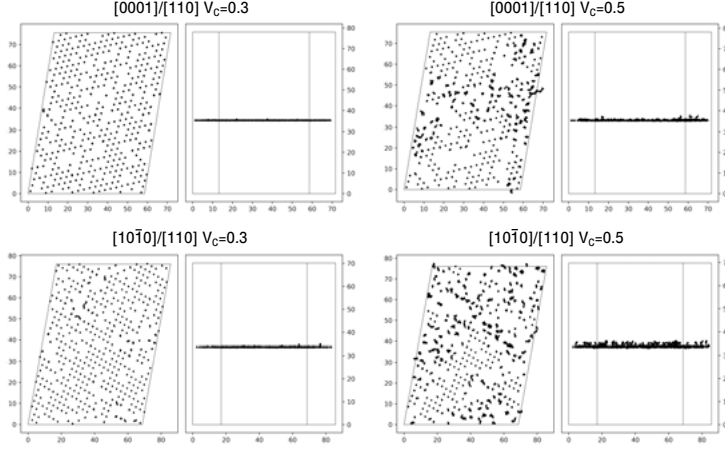


Figure 6.1. All diffusion results, filled markers indicate the 2500 ps run and the open markers indicate the 500 ps runs.

the C depletion increases and the temperature increases. Though for the lower levels of C depletion, 10% and 30%, diffusion events are very rare and in many cases non-existent. Looking at the trajectories of the C atoms in the various simulations it can be seen that the interfaces are almost completely stable up to C depletions of 30% for temperatures at or below 1373 K. A selection of this is shown in figure 6.2 which is representative for all interfaces. It is also seen that when C atoms starts to diffuse away from their initial sites it tends to happen in clusters and regions leaving other areas almost unaffected.

Quantifying the ratio of atoms that are diffusing by defining a criteria of movement extending more than 3/4 of the nearest neighbour distance for the C atoms the overview in figure 6.3 is arrived at. It shows the fraction of the total number of C atoms in the outermost layer that are diffusing based on the criteria defined above in each simulation. As was stated previously at low C depletions almost nothing happens, which might be expected as the behaviour of the interfaces at low C depletions should converge to the behaviour of the pristine interfaces. More interesting is the behaviour for depletions of 50% and above, as there, diffusion of C atoms becomes common at temperatures expected in the cutting zone. Suggesting a progression of wear that for each layer start slowly and then picks up speed as more and more C atoms gets removed. Looking at figure 6.3 it seems that the C atoms in the prismatic interfaces are slightly more mobile than the C atoms in the basal interfaces which would be expected based on the initial diffusion barriers however this difference is much smaller than the large initial difference in barriers would



*Figure 6.2.* Trajectories for the C atoms in the basal (top) and prismatic (bottom) interfaces against the [110] surface of BCC W for C depletions of 30% and 50% at 1173 K in the 2500 ps run.

suggest. A summary of the results for the 50%, 70% and 80% depletions can be found in table 6.2 where the lower depletions are left out due to the low number of diffusion events. Based on the fact that the barriers between the 50% and 70% depletions drop only slightly while the number of diffusing C atoms increases quite a bit the removal of C from the interfaces likely does not lower the diffusion barriers in any general sense but rather increases the chances of any one C atom residing in a low barrier site, possibly coinciding with regions where W from the C depleted WC start to form a BCC coordination, allowing it to escape its initial location more easily. This would also explain why the barriers become essentially similar between the basal and prismatic interfaces.

**Table 6.2.** Pre-factors,  $D_0$  ( $\text{m}^2/\text{s}$ ), and activation energies,  $\Delta E$  (eV), calculated from the fits made to the diffusion rates for the different C depletions.

C depletion WC/W	50%		70%		80%	
	$D_0$	$\Delta E$	$D_0$	$\Delta E$	$D_0$	$\Delta E$
[0001]/[100]	9.4E-11	0.47	6.6E-11	0.32	6.8E-11	0.31
[0001]/[110]	3.2E-11	0.44	1.5E-11	0.26	1.5E-11	0.25
[0001]/[111]	1.2E-11	0.35	4.6E-11	0.30	5.1E-11	0.29
[10-10]/[100]	7.9E-11	0.38	4.0E-11	0.26	6.0E-11	0.29
[10-10]/[110]	4.2E-11	0.39	5.4E-11	0.31	4.0E-11	0.28
[10-10]/[111]	5.0E-11	0.39	6.7E-11	0.32	5.8E-11	0.29

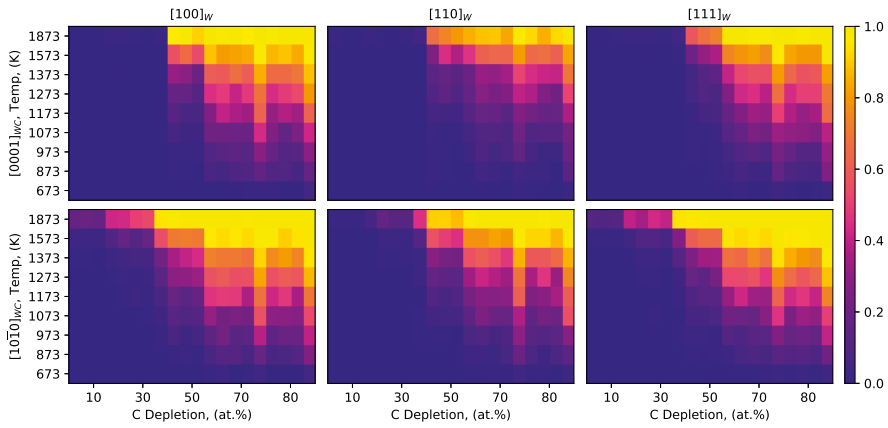


*Figure 6.3.* Ratio of mobile C atoms to all C atoms in the outermost C layer of the WC. Criteria set for classification of a mobile C atoms is a movement extending more than  $3/4$  of the nearest neighbor distance for C in WC.

## 7. Tools for Finding, Building and Analysing Interfaces

Paper III is different from the rest of the papers as it does not directly focus on the specific application of wear in WC materials but rather describes the process of building a computational tool kit to facilitate easy construction and calculation of surface and interfacial properties. The result is a python package [73] that allows easy construction of interfaces and interface datasets and convenient containers to handle not just singular matches but rather the entire space of discovered interfaces making the task of screening unknown interface systems simple. Included are also analysis and visualization tools to provide fast and easy overviews of various parameters related to the interfaces.

### 7.1 Concept

The process of building interfaces for use in computations can be both tedious and non-trivial. If the goal is to build a specific interface match between given base structures some simple scripts are usually enough. If the goal is to build the most suitable interfaces possible, subject to some constraints, tools are needed to search through the set of possible interface matches between the base structures. This is the approach taken in the first and second papers and have been done using the VNL software package [70]. Other software packages exist that does this as well but as they are commercial programs they tend to come with a price tag as they are often bundled with a lot of other functionality. Further, if the goal is to investigate an unknown interface system, e.g. WC/W, it is of interest to look at large sets of interfaces to see the trends that exist and allow that to strengthen any conclusions drawn in regards to the system by seeing the properties of the individual interfaces placed in a larger context. For this approach tools are needed to not only find possible interface matches but to be able to work with and manage the full interface datasets allowing for fast and easy ways to find, analyse, sort, remove and export individual interfaces in a way that can be implemented in screening workflows. This task requires purpose built functionality beyond what is available. The python package developed here, *interfaceBuilder*, focuses on the this last approach but as the previously described use cases can be considered special situations of the same approach it works equally well there. The package lets the user supply 2 base structures from which all lowest strain interface matches are



found. All interface matches can then be analysed and compared using simple plotting functions and constructed as desired with respect to repetitions, vacuum layer, interface distance, relative translations, etc. and exported to common simulation file formats in a way suitable for use in screening calculations allowing the user to build up sets of properties that fully describe any interface system of interest.

## 7.2 Application and Capabilities

The starting point for any use case is to define the starting base structures that will make up the interfaces. The package allows the user to load base atomic structures from either of the structural formats used by the common simulation programs VASP, LAMMPS and EON [15–17, 34, 47] or to define the structures manually. The base structures are then used as inputs to build a dataset of interface matches between the structures subject to any limitations specified by the user regarding system size, shape, strain and relative rotation. In the default implementation the method for finding interface matches is the one described by [69] with the strain between the surfaces calculated as

$$\epsilon_{11} = \left| \frac{a_{1,x}}{b_{1,x}} \right| - 1 \quad (7.1)$$

$$\epsilon_{22} = \left| \frac{a_{2,y}}{b_{2,y}} \right| - 1 \quad (7.2)$$

$$\epsilon_{12} = \frac{1}{2} \frac{a_{2,x} - \frac{a_{1,x}}{b_{1,x}} b_{2,x}}{b_{2,y}} \quad (7.3)$$

$$\epsilon_{mas} = \frac{|\epsilon_{11}| + |\epsilon_{22}| + |\epsilon_{12}|}{3} \quad (7.4)$$

with  $a_{i,j}$  and  $b_{i,j}$  representing the  $x$  and  $y$  components ( $j$ ) of the first and second cell vectors ( $i$ ) of the bottom and top surfaces respectively and with  $\epsilon_{mas}$  as a measure of the mean absolute strain. The method matches all permutations of the base cell vectors of the top base cell between  $[-n_{max}, n_{max}]$  for the first cell vector and  $[0, m_{max}]$  for the second cell vector to the best possible strain matches of the bottom base cell at each angle of relative rotation between  $[0, 180)$  degrees in increments of  $d\theta$  resulting in a raw dataset of  $((2 * n_{max} + 1) * (m_{max} + 1))^2 * 180 / d\theta$  total combinations. After removal of duplicate interfaces and interfaces with properties outside of any user specified limitations the dataset is ready. Figure 7.1 shows the results of an interface

search between base cells of BCC W oriented with directions [100] and [110] parallel to the z-direction along with an automated criteria for removal based on the number of atoms and strain in the interfaces.

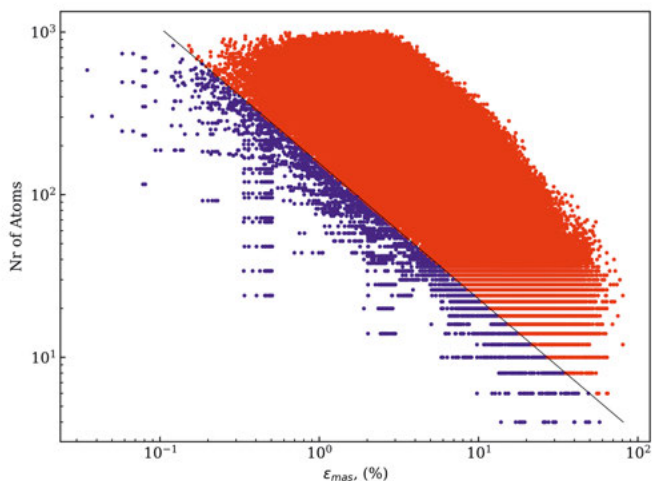


*Figure 7.1.* Unique interface combinations found for a search between differently oriented cells of BCC W. Showing an automated criteria for removal based on a boundary limit between the number of atoms and the mean strain.

From here the full set of interfaces can be compared and analysed based on parameters available at this stage, with these parameters representing the geometric properties of the interfaces such as number of atoms, strain, cell shape and size etc. The interfaces can be further worked to remove specific unwanted interfaces, sorted, updated to change elemental terminations, and any specific interface can be visualized to show the exact match and summary information can be printed for specified interfaces. Figure 7.2 shows a specific interface match from the dataset shown in figure 7.1 along with an image of the same interface exported in a VASP POSCAR format and visualized in VESTA [74]. Both interfaces and surfaces can be exported and the surfaces can be exported either unstrained or strained to match the shape and size they would have as part of the specific interface.

Often the most relevant analysis and comparisons between interfaces are the ones made based on energetic properties such as the work of adhesion or the interfacial energies. These require calculation using 3<sup>rd</sup> party software such as VASP or LAMMPS but one of the main points of this package is to allow for quick and easy analysis of these properties combined with the properties already available and as such functions for importing these values after calculation exists after which they can be accessed using predefined keywords just as all other properties.

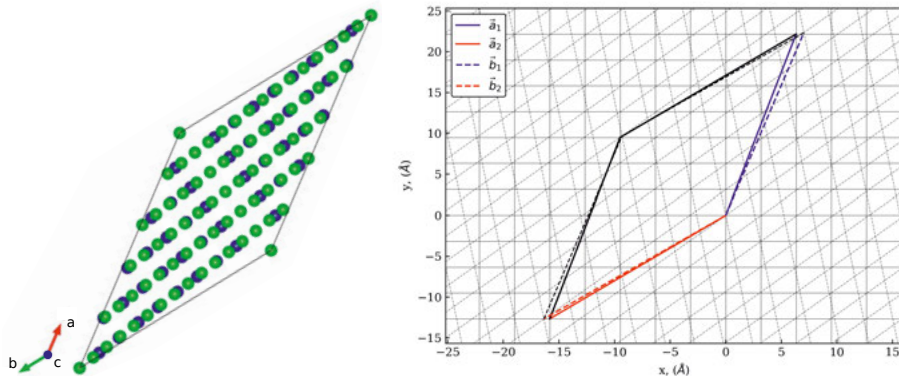


Figure 7.2. Example interface match from the dataset shown in figure 7.1 along with the structure exported in a VASP POSCAR format and visualized in VESTA [74].  $\vec{a}_1$ ,  $\vec{a}_2$ ,  $\vec{b}_1$  and  $\vec{b}_2$  are the first and second cell vectors of the bottom and top surfaces that are matched to form the interface.

Additionally the package is built with the intention of allowing easy comparisons between properties calculated using different levels of theory, i.e. first screening energetic properties using a classical potential in LAMMPS and then doing the same for a subset in VASP and comparing the results. In order to make this possible and allowing good comparisons to be made the differences that normally exist between the structural properties of the base cells as calculated by the different methods must be considered as these differences will lead to different strains when the same interfaces are calculated using different methods. For this purpose a second set of base cell vectors can be loaded and if specified when exporting an interface the interface structure is scaled to reflect this alternative base. Figure 7.3 shows a comparison between the  $\epsilon_{mas}$  parameter for the two different sets of basis vectors that arise after relaxation of the base cells using LAMMPS and VASP for the W/W dataset used as an example here, it also shows a comparison between the calculated values for the work of adhesion,  $W_{ad}$ , between LAMMPS and VASP. The difference seen between the two match rather well the difference seen in calculations of the surface energies as the ABOP underestimates them for the BCC W surfaces and it transfers through to the  $W_{ad}$  parameter, values for the surface energies of the BCC W surfaces discussed here can be found presented together with the surface energies of a number of WC surfaces in the following chapter.

As the relative translation between the individual surfaces making up the interface can be of interest when studying the energetic properties this too can be specified when an interface is exported. Specific details of the different use cases are further presented when discussing paper IV where this package is used to perform a large scale investigation of interface parameters in several WC/W interface systems.

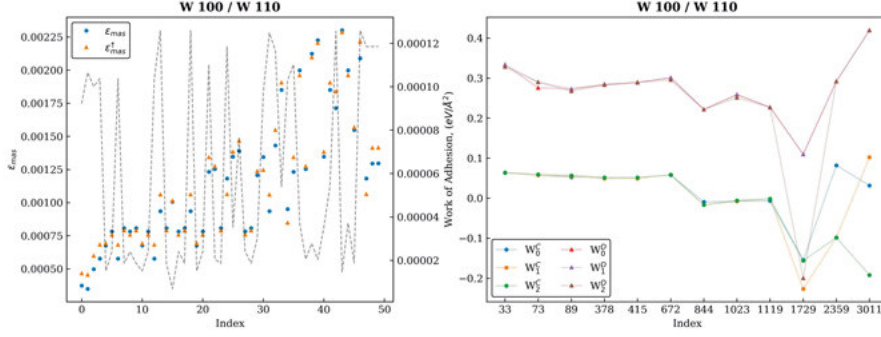


Figure 7.3. Comparison between the mean absolute strain,  $\epsilon_{mas}$ , in the two different basis (left) and a comparison between the VASP ( $W_i^D$ ) and LAMMPS ( $W_i^C$ ) results for the  $W_{ad}$  at different translations (right).

As a final overview figure 7.4 shows some examples of analysis which can be made and properties which can be accessed and plotted simply by supplying convenient keywords. It shows examples of various graphical representations and correlation analysis which can be made between any and all properties. The top left and top right figures shows property plots which allow for the visualization of any pair of properties or pairs together with an additional property as a color scale. Properties in the specific sub figures are the interface cell angle  $a_1 \angle a_2$  against  $\epsilon_{mas}$  (top left) and  $W_{ad}$  at all translations against the maximum strain component in the interface with the ratio of base cells making up the interfaces as a color scale (top right). The bottom left shows a histogram of the  $W_{ad}$  for the 3 different investigated translations as calculated in LAMMPS for the example W/W interface set used here with values shifted in the y direction for clarity. Finally the bottom right figure shows the matrix of Spearman correlation coefficients between all the specified parameters which are  $W_{ad}$  for the first translation ( $W_0^C$ ), the maximum difference in  $W_{ad}$  between different translations ( $\Delta W^C$ ), the density of atoms parallel to the interface due to strain ( $\rho$ ), the number of atoms (Atoms), the maximum strain component ( $\text{Max}(\epsilon_{11}, \epsilon_{22}, \epsilon_{12})$ ), the average strain component ( $\epsilon_{mas}$ ), the interface area (Area), the minimum width of the interface ( $\text{Min}(x^C, y^C)$ ) and the length of the first interface cell vector ( $a_1$ ). Though mainly as an example, some obvious correlations and inverse correlations can be seen e.g. the inverse correlation between  $\epsilon_{mas}$  and the area. Many additional properties exist along with the ability to supply user defined values.

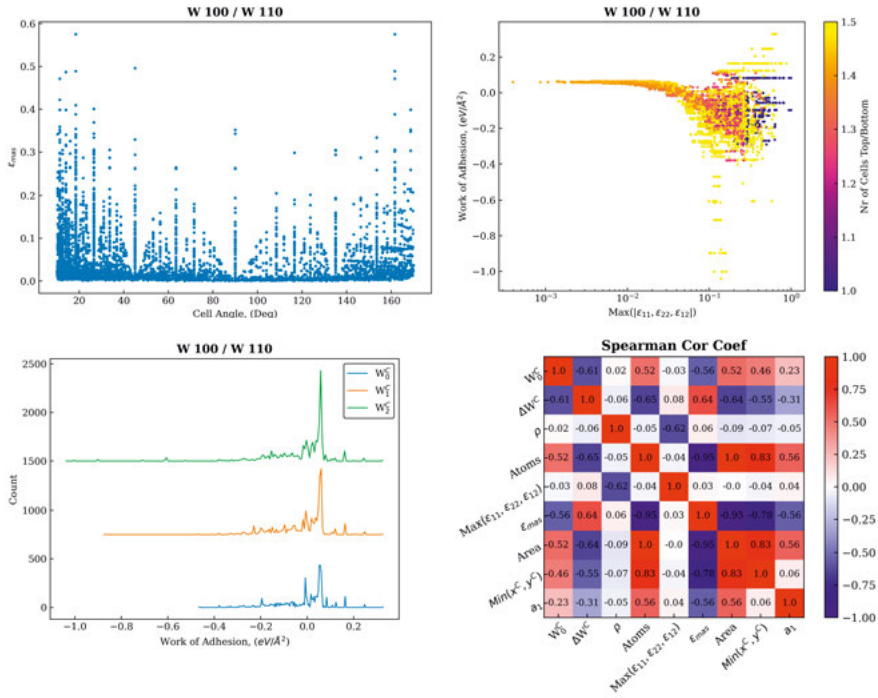


Figure 7.4. Examples of analysis and visualizations easily accessible through simple keywords. See the text for a complete description of all entries.

## 8. Large Scale Screening of WC/W Interface Parameters

In previous papers, I and II, the interfaces used in the investigations of C diffusion have been interfaces built considering mainly strain and system size with the interface combinations focusing on having both a prismatic and a basal WC termination without any deeper investigation into which interfaces might be expected. In paper IV using the tools developed in paper III, a large scale screening of interface parameters for different WC/W interface systems were done using both a classical approach with the ABOP [37] in LAMMPS [34] and first principles in VASP-VTST [15–18]. The results include the work of adhesion and interfacial energies of a large number of WC/W interfaces as a function of strain and system size where the preferred interface combination is found to be the W terminated  $[10\bar{1}0]$ -I/[110].

### 8.1 Computational Approach

Three different cells of WC terminated by the basal, prismatic type-I and prismatic type-II planes and two different BCC W cells, terminated by the [100] and [110] planes were selected and fully relaxed in LAMMPS. Using the *interfaceBuilder* python package developed in paper III, interface datasets containing the lowest strain interface matches between the relaxed WC and W structures were created with the WC as unstrained bottom surfaces and the BCC W as strained top surfaces. The matches were restricted to permutations of the cell vectors of the BCC W cells using an  $n_{max}$  and  $m_{max}$  of 12 and increments of relative rotation,  $d\theta$ , of  $2^\circ$  as described in paper III. This resulted in 6 different interface systems containing a little less than 1,000,000 unique interfaces each. To reduce this to a manageable size and still retain the most relevant cross section of interface combinations a limiting boundary was constructed for each system between the number of atoms,  $N_{atoms}$ , in each interface and the mean absolute strain,  $\epsilon_{mas}$  which is defined in equation 7.4, as

$$N_{atoms} = A\epsilon_{mas}^B \quad (8.1)$$

where the  $A$  and  $B$  parameters were found by fitting the data to the lowest strain interface match overall and the lowest strain interface match of the interfaces containing the fewest number of atoms. The value of the  $A$  parameter was then increased until 5000 interfaces were included in each of the interface systems,

see figure 7.1 for an equivalent treatment of the system considered there. As the matching of interface parameters are defined only by the geometry of the cells and the WC cells have alternating elemental terminations on the top and bottom cell surfaces when stoichiometry is kept the total number of interface systems were expanded from 6 to 12 by including both C and W terminations of the interface-facing surfaces of the WC cells by simply interchanging the C and W atoms.

For all interface systems the work of adhesion, both against unstrained and strained surfaces as to include and exclude the effects of strain, were calculated for all interface matches at 4 different initial relative translations, see figure 8.1, using LAMMPS as described in equation 3.9.

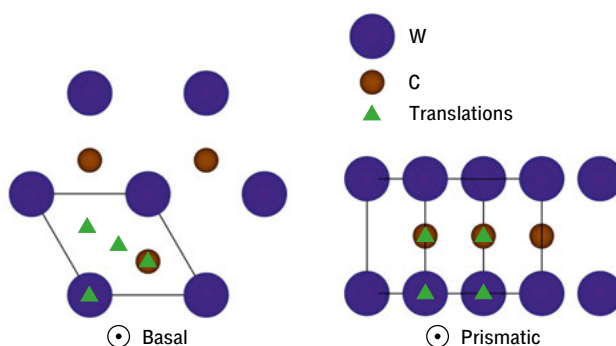


Figure 8.1. Relative translations investigated

For a subset of interfaces the same calculations were then repeated in VASP, see table 8.1 for a complete set of calculations. This was then followed by calculations of the surface energies for all 8 unique surfaces present in the interface systems in both LAMMPS and VASP following equations 3.5 and 3.8. In the case of the stoichiometric surfaces the chemical potential at the W rich end were used in the calculations and for the prismatic WC surfaces the surface energies were calculated as in [37] by considering the ratio between the C and W terminations to be the same for the type-I and type-II terminations. Finally the interfacial energies were calculated using the surface energies and the work of adhesion with strained references according to equation 3.10.

As can be seen in table 8.1 VASP calculations were done only for the W terminated WC cells except for the [0001]/[100] interface where the C termination was included as well. The reason for this being that the W termination is expected to be the energetically preferred termination [58, 60] in these environments. The single above mentioned C termination was included for completeness but the computational cost for the DFT calculations were not deemed to merit such calculations for all interface systems. Both terminations were included in the LAMMPS calculations as those are much less demanding.

**Table 8.1.** *Interface combinations and the number of calculations of the work of adhesion and interfacial energies performed, x4 indicates the number of relative translations, along with the number of atomic layers used.*

Interface	LAMMPS	VASP	Layers
$[0001]^C/[100]$	5000 x4	41 x4	6/6
$[0001]^W/[100]$	5000 x4	56 x4	6/6
$[0001]^C/[110]$	5000 x4	-	6/6
$[0001]^W/[110]$	5000 x4	46 x4	6/6
$[10\bar{1}0]^C\text{-I}/[100]$	5000 x4	-	8/6
$[10\bar{1}0]^W\text{-I}/[100]$	5000 x4	44 x4	8/6
$[10\bar{1}0]^C\text{-I}/[110]$	5000 x4	-	8/6
$[10\bar{1}0]^W\text{-I}/[110]$	5000 x4	27 x4	8/6
$[10\bar{1}0]^C\text{-II}/[100]$	5000 x4	-	8/6
$[10\bar{1}0]^W\text{-II}/[100]$	5000 x4	42 x4	8/6
$[10\bar{1}0]^C\text{-II}/[110]$	5000 x4	-	8/6
$[10\bar{1}0]^W\text{-II}/[110]$	5000 x4	25 x4	8/6

## 8.2 Results and Discussion

The results for the calculation of the work of adhesion against unstrained surface slabs are shown in figure 8.2. The color scale in the figures described the ratio between the number of cells in the top and bottom surfaces,  $N_{top}/N_{bottom}$ , as an indication of the match between the base cells in the interfaces. This ratio converges at the low strain end to the inverse value of the relative areas,  $A_{Bottom}/A_{top}$ , and as it is completely described by the geometry of the interfaces four different groups exist as the type-I and type-II WC surfaces have the same geometries for their interface matches. At the high strain end this ratio shows clear discrete levels which can be useful in interpreting the results. The reason for the clear steps is the strong inverse correlation that exists between the strain and the system size, i.e. the smaller systems have larger strains while the larger systems have lower strains, and as the interface matching is done purely based on strain the ratio changes abruptly as the best strain match goes from being e.g. 1:1 to 1:2 etc. As the results show the difference in energy between the slabs in their relaxed states and the interfaces the strain contributions are included. This contribution is dependent on the height of the strained top layer and including more layers will increase the negative penalty for larger strain matches. Opposing this destabilisation is the bonding in the interface which instead stabilises it, this contribution is not dependent on the height of the strained surface and as such will be overstated unless a representative number of strained layers are included. In this specific application the total height of the top W layer is measured at around 100 nm [11] and even if the thickness of the top layer would be smaller it would still require thicknesses much larger than what could realistically be included in calculations to



be well described as a 10-20 nm layer still requires roughly 30-60 layers of atoms. Given this and the fact that the results, even with this very thin top layer, show a clear trend of lower work of adhesion against higher strains it is suggested that the correct interface combinations indeed will be the ones found at the low strain end. At the low strain end the results using either unstrained references, as discussed above, or using strained references, as also calculated, give the same results, both in the case of the LAMMPS calculations and the VASP calculations.

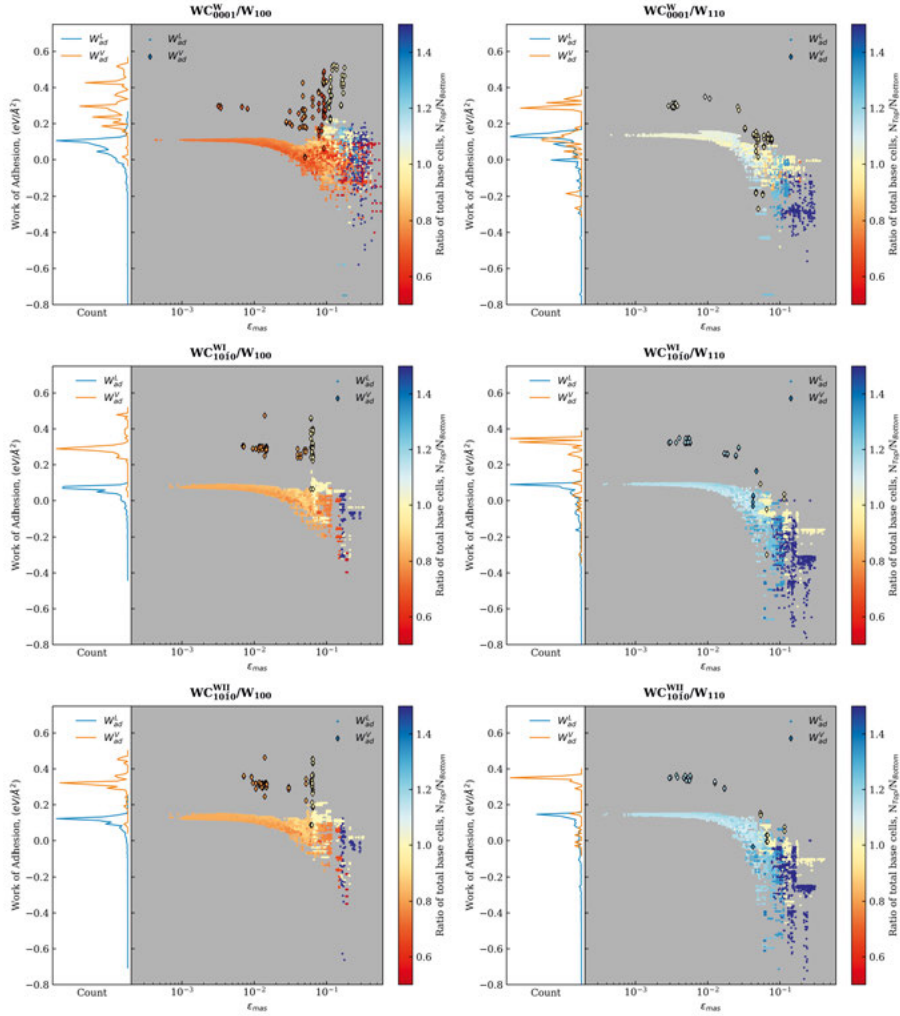


*Figure 8.2.* The work of adhesion plotted against the mean absolute strain for all W terminated interfaces and translations with the ratio between the total number of base cells in the top and bottom surfaces as a color scale. Lammmps values as dots and VASP values as diamonds.

Looking at the values for different translations the difference quickly drops to zero as the size of the interface increases. This being attributed to the fact that a larger interface means that the positioning of the atoms in the interface will average out over many different sites.

Comparing the values between the LAMMPS and VASP calculations the difference is stable at low strains but gets worse as the strain increases as can be seen in figure 8.3. Though the stability of the difference is likely not mainly related to the strain but rather to the fact that low strains correlate with larger interfaces leading to a stable average value as opposed to the smaller higher strain interfaces where the higher level of detail in the VASP calculations become clearer.

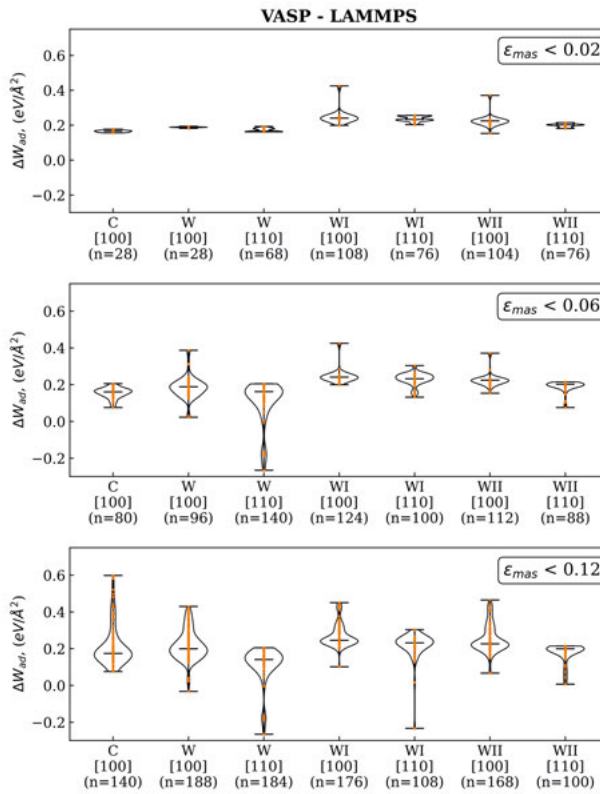


*Figure 8.3.* Difference between VASP and LAMMPS data at strains below, 0.02, 0.06 and 0.12 respectively. Distribution of differences and all individual datapoints with sample size indicated. C, W, CI, WI, CII and WII represents the C and W terminated basal, type-I and type-II surfaces respectively, [100] and [110] denote BCC W surfaces

The results for the surface energies as calculated in both LAMMPS and VASP are shown in table 8.2. These results can in part be compared to the results found in [37, 58, 60] and changing the value of the chemical potential

to match where appropriate the results agree well. Looking at the results the justification for focusing on the W terminations in the VASP calculations are supported as the surface energies of the C surfaces are higher than the equivalent W terminations in all cases. Additionally it can be seen that the values for the surface energies calculated in VASP tend to be higher across the board with the exception of the basal WC terminations. This difference is likely the reason for the higher overall values observed in the work of adhesion as well when using VASP.

**Table 8.2.** Surface energies for all considered surfaces including the difference between VASP and LAMMPS, units are  $\text{eV}/\text{\AA}^2$ .

Surfaces	LAMMPS	VASP	$\Delta$
$\sigma_{[100]}$	0.09	0.25	0.16
$\sigma_{[110]}$	0.06	0.21	0.15
$\sigma_{[0001]}(C)$	0.39	0.38	-0.01
$\sigma_{[0001]}(W)$	0.17	0.21	0.04
$\sigma_{[10\bar{1}0]}(CI)$	0.20	0.27	0.07
$\sigma_{[10\bar{1}0]}(WI)$	0.09	0.19	0.10
$\sigma_{[10\bar{1}0]}(CII)$	0.44	0.52	0.08
$\sigma_{[10\bar{1}0]}(WII)$	0.20	0.36	0.16

The median interfacial energies for the 50 (5) lowest strain interfaces as calculated in LAMMPS (VASP) are shown in figure 8.4, the results include all 4 translations in every case.

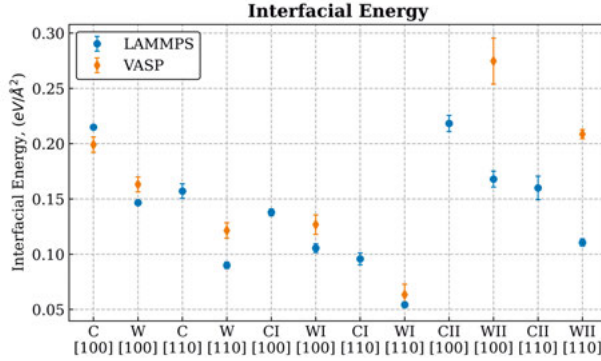


**Figure 8.4.** The median interfacial energy of the 50 (5) lowest strain interfaces ( $\pm\sigma$ ) for all interface systems as calculated in LAMMPS (VASP). C, W, CI, WI, CII and WII represents the C and W terminated basal, type-I and type-II surfaces respectively, [100] and [110] denote BCC W surfaces.

The interfacial energies were calculated using the strained surface reference calculations for the work of adhesion however as the results presented here are based on the lowest strain interfaces, following the discussion in the previous

section, the results are the same as they would be using the unstrained surface references. Based on the result the  $[110]$  surface terminations of the BCC W are favoured over the  $[100]$  terminations for all equivalent interfaces and the type-I prismatic terminations are strongly favoured over the type-II terminations. Additionally, for all calculations where data is available for the C terminations the equivalent W termination is preferred further justifying the focus on the W terminations. Overall the preferred interface combinations are the W terminated  $[10\bar{1}0]$ -I/ $[110]$  and  $[0001]$ / $[110]$  based on both the LAMMPS and VASP data. Overall the trends between the LAMMPS and VASP data agree well.

## 9. KMC Simulations of C Diffusion

In paper V the diffusion of C in WC/W interfaces was revisited using kMC. Due to the observed stability of the WC/W interfaces the use of MD, as discussed at length, is not a suitable method to estimate the rates of diffusion in pristine WC/W interfaces, to get around this kMC was used. The  $[10\bar{1}0]/[100]$  interface used in paper I was investigated and the rate of C diffusion estimated by calculating the MSD of diffusing C atoms at different temperatures. The results show an activation energy and diffusion pre-factor in the interface of  $\Delta E = 1.24 \pm 0.23$  and  $D_0 = 1.8 \times 10^{-8} \pm 4.8 \times 10^{-8}$ . From the trajectories of the C atoms it is observed that the preferred place of diffusion is within the interface with the bottom of the BCC W dictating in which directions this diffusion occurs, the same is found for the  $[10\bar{1}0]/[110]$  interface.

### 9.1 Computational Approach

Two interface combinations were investigated in this project,  $[10\bar{1}0]/[100]$ , which is the same interface as was used in paper I and  $[10\bar{1}0]/[110]$  which was built using the *interfaceBuilder* software package. The choice of interfaces were made considering the interfacial energies for the different interface combinations as calculated in paper IV and for the  $[10\bar{1}0]/[100]$  interface, based also on the large set of available DFT data from paper I to which the results could be compared. A summary of both interfaces can be seen in table 9.1.

To ensure that the interfaces used were in their most stable configurations prior to the kMC simulations the interfaces were run using classical MD in LAMMPS [34] with the ABOP [37] for 10 ns at a temperature of 1173 K using a Nose-Hoover thermostat [71, 72]. To enforce bulk WC distances and a stable base for the simulations the bottom 3 layers were frozen. The results showed, in line with previous results, that the interfaces were stable and that no additional relaxation of the interfaces occurred and as such relaxed in preparation for the kMC simulations.

The EON software [47] was used for the kMC simulations and the mode of running was the Adaptive Kinetic Monte Carlo mode in which the event table

**Table 9.1.** *Summary of investigated interfaces.*

WC/W	Length a/b, (Å)	Strain a/b, (%)	Layers	Atoms
$[10\bar{1}0]$ -I/ $[100]$	11.45/11.24	2.12/-0.59	(5, 5), 7	251
$[10\bar{1}0]$ -I/ $[110]$	23.33/8.43	0.32/2.60	(4, 4), 6	354

at each reactant is built during the simulation. Finding the rates consists of locating the TS in some suitable way and then using HTST [49] to calculate the attempt frequencies. Finding the TS can be done in several different ways but here the dimer method [53] was used. In practice this works by initiating a large number of dimers by randomly displacing specified atoms and their surrounding and from there letting the dimers work their way towards whichever TS they might find. When the ratio of new TS found and repeat TS found meet the desired set criteria the rate table is considered complete. Together with the calculated attempt frequencies the system is then ready to take a kMC step after which the process begins again. Here the random displacement was applied to a single C atom in the outermost WC layer and all atoms within 2.4 Å of that C, the criteria for the completeness of the rate table was set to 0.95.

All simulations were run for a minimum of 5000 kMC steps resulting in total simulation times ranging from tens of  $\mu\text{s}$  to tens of ms. The full set of simulations can be seen in table 9.2.

**Table 9.2.** Overview of all simulations, showing temperature, number of steps and the total simulation time.

Interface	Temperature, (K)	Steps	Time, (s)
[10 $\bar{1}$ 0]-I/[100]	1173	5435	$5.29 \times 10^{-5}$
[10 $\bar{1}$ 0]-I/[100]	1073	5005	$5.20 \times 10^{-5}$
[10 $\bar{1}$ 0]-I/[100]	973	5143	$2.24 \times 10^{-3}$
[10 $\bar{1}$ 0]-I/[100]	873	5626	$1.46 \times 10^{-2}$
[10 $\bar{1}$ 0]-I/[110]	1173	5275	$6.26 \times 10^{-5}$
[10 $\bar{1}$ 0]-I/[110]	1073	5106	$5.48 \times 10^{-3}$

Since the timesteps in kMC simulations are unequal the calculation of the MSD is a bit more complicated than compared to the case of equal timestep simulations. To deal with this all time differences and all corresponding spacial differences from the trajectories of the diffusing atoms were calculated and placed in bins based on the time difference. The spacial values in each bin were then averaged and the linear fit of the MSD were made to the average values of the bins. Additionally, as the averages were made up of different numbers of values the linear fits were weighted by the number of entries in each bin.

## 9.2 Results

For the [10 $\bar{1}$ 0]-I/[100] interface the simulations resulted in the discovery of 3,897 unique reactant states containing 50,846 processes, while for the [10 $\bar{1}$ 0]-I/[110] interface, 1279 reactant states were found containing 17,930 processes. The diffusion barriers and the attempt-frequencies for all processes in both interfaces are shown in figure 9.1.

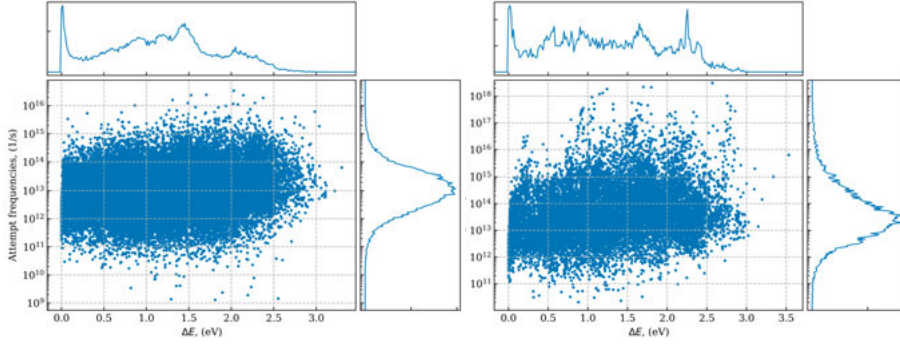


Figure 9.1. Diffusion barriers and attempt frequencies found for the  $[10\bar{1}0]$ -I/[100] interface (left) and  $[10\bar{1}0]$ -I/[110] interface (right).

Comparing the distribution of values for the barriers and attempt frequencies between the two interfaces they are fairly similar, as might be expected based on the equal WC structure in both cases, but with a slight, about 0.15 eV, shift in the barrier distribution towards higher energies for the  $[10\bar{1}0]$ -I/[110] interface. The bulk of the distributions for the attempt frequencies lie in the 1-100 THz range for both but the values for the  $[10\bar{1}0]$ -I/[110] interface tend to scatter a bit more.

The trajectories of the diffusing C atoms for both interfaces can be seen in figure 9.2. Focusing on the  $[10\bar{1}0]$ -I/[100] interface it is clear that the C diffusion favours the interface and the immediate bottom of the BCC W. This is attributed to the high chemical potential of C in BCC W and relaxing a C atom in octahedral sites in the BCC W results in an energy penalty as  $0 \rightarrow 0.82 \rightarrow 2.17 \rightarrow 1.8 \rightarrow 2.93$  (eV) when moving further into the pure W as compared to the pristine interface, this was observed in paper I as well and can be seen there in figure 5.5. It is also clear that for this interface the diffusion directions of the C within the interface is set by the W atoms in the BCC W, while the W atoms in the WC seem to have little impact on this. Calculating the nearest neighbour distances for the C within the interface it is found that the C mostly resides surrounded by 4 roughly equidistant W atoms, this behaviour together with the directions of the diffusion all match well with the observations made in paper I. For the  $[10\bar{1}0]$ -I/[110] interface the diffusion of the C is again contained to the interface as might be expected. Here, the bottom of the BCC W seems to restrict the movement of the C to within the rows formed together with the WC resulting in the diffusion following linear paths, this is likely not a general behaviour but specific to this interface match and dependent on how the WC and BCC W lines up.

The diffusion values as calculated from the MSD lead to estimates of the diffusion pre-factor of  $D_0 = 1.8 \times 10^{-8} \pm 4.8 \times 10^{-8}$  m<sup>2</sup>/s and an activation energy of  $\Delta E = 1.24 \pm 0.23$  eV for the  $[10\bar{1}0]$ -I/[100] interface. The calculated

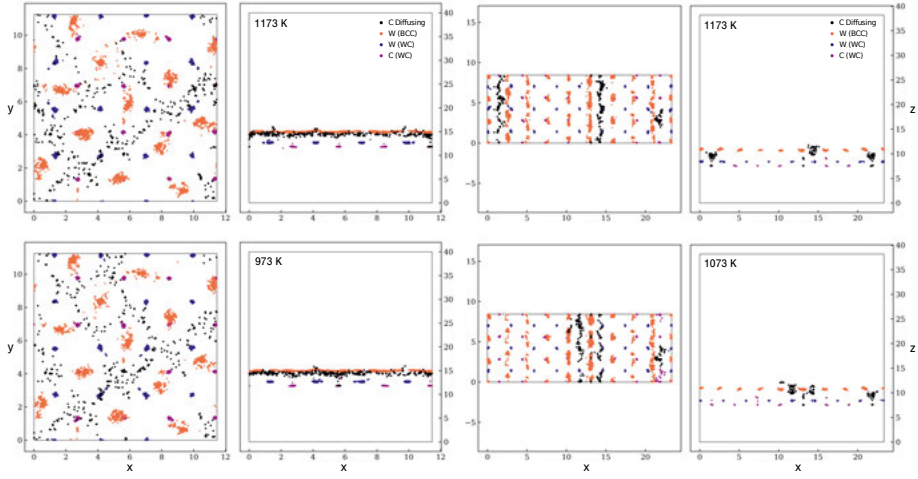


Figure 9.2. Trajectories of the diffusing C atoms in the 1173 K and 973 K simulations for the  $[10\bar{1}0]$ -I/ $[100]$  interface (left) and at 1173 K and 1073 K for the  $[10\bar{1}0]$ -I/ $[110]$  interface (right).

MSD curves and the resulting fit of  $\log(D)$  against  $1/T$  can be seen in figure 9.3.

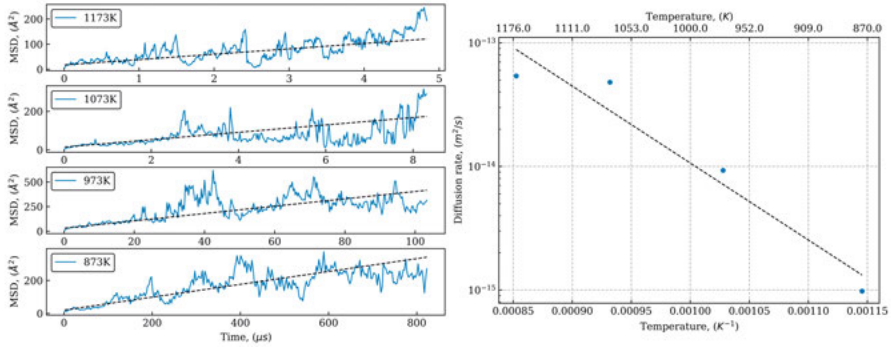


Figure 9.3. MSD curves for the diffusing C atoms (left) and the fit of  $\log(D)$  vs.  $1/T$  (right) for the  $[10\bar{1}0]$ -I/ $[100]$  interface.

Comparing these values against the values for the elementary rates calculated in paper I the value for the diffusion barrier agree fairly well considering the range of values in paper I with most lying between 1.23-1.48 eV with some values at 0.84 eV. The same is roughly true for the diffusion pre-factor with the values from paper I in the region of  $10^{-7}$  m<sup>2</sup>/s, but it should be considered that the calculation of the pre-factor is very sensitive to the values used in the linear fit. Further, as a straight comparison a group of elementary rates and the overall diffusion rate is not the same thing. For the kMC simulation the expectation is that the description of the possible processes is much more complete



and as such would give a better picture of the diffusion, while the uncertainties mostly lie in the ability of the ABOP to correctly describe the diffusion process. However, if the elementary rates can be considered to be somewhat representative for the interface as a whole the results should point in the same direction, which they do. It seems that the ABOP gives a reasonable result for both for the diffusion values as well as the overall diffusion behaviour within the pristine interface.

Overall the results should lead to further investigations of the diffusion processes within WC/W interfaces using kMC as the method can provide interesting complementary insights and results to both DFT and MD results.

## 10. Summary and Outlook

This work aims at trying to explain the processes behind the high wear rates observed in Ti-alloy turning using WC/Co tools. This process is orders of magnitude faster than when machining e.g. steel and it is one of the hurdles that need to be overcome for a broader use of Ti-alloy materials in non-specialty applications. The issue is attributed primarily to the poor thermal conductivity of Ti which raises the temperature in the cutting zone well above what is seen in steel machining making the wear contribution from diffusion more pronounced as it is exponential in relation to temperature, additionally Ti is very reactive with the tool materials at elevated temperatures. These two factors lead most to conclude that some form of dissolution/diffusion of tool material is taking place. In this work the attention has been focused on the observed depletion of C in the outermost WC grains and the WC/W interfaces created by this as the rates in this depletion process likely play an important role in explaining the wear behaviour.

This work contains two different areas of focus, the diffusion of C in WC/W interfaces and the properties of those same WC/W interfaces. Focusing first on the diffusion of C, it has been studied using 3 different approaches, DFT, MD and kMC, attempting to use the most suitable tools available to describe the processes at different timescales and system sizes covering different stages of the C diffusion and depletion process.

The initial depletion of C was investigated using DFT by means of HTST, NEB and the Dimer method. Where diffusion paths into and within WC/W interfaces were examined and quantified by attaining values for the activation energies and the pre-factors as well as a qualitative understanding of the diffusion paths most easily accessible to the diffusing C. Results showed fairly similar values for the diffusion within the interfaces but a large difference in activation energy between the basal and prismatic planes of the WC. This difference is something that is not seen, at least not as clearly as the energetics would dictate, in observations.

The dynamics of the C diffusion as a function of temperature and level of C depletion was studied using MD with a classical force field approach to overcome the size and time limitations present in DFT. By calculating the MSD the diffusion of C was studied for 6 different interface systems as a function of C depletion in the outermost WC layer. The results showed that for C depletions up to 30% all interfaces were stable just as in their pristine states. At 50% C depletion the activation energy had dropped to around 0.4 eV for all interfaces, both basal and prismatic, showing that the clear difference in activation

energy seen in pristine interfaces were no longer present, a minor additional drop in activation energies were seen for depletions of 70% but no additional decreases were seen beyond that point. The vanishing of the difference between the basal and the prismatic interfaces and the accelerated diffusion rate as a function of C depletion might explain why directional preferences are not clearly seen in WC grains in worn inserts and why the otherwise very stable WC can get worn so quickly.

To bridge the divide between C diffusion in the pristine interfaces examined by DFT and the C depleted interfaces examined using classical MD as well as extending the timescales into the  $\mu$ s-ms range, kMC was used. The approach taken was one using Adaptive Kinetic Monte-Carlo allowing the system at each diffusion step to map out any possible transition states on the fly which was made possible by the use of the classical ABOP. The results from the trajectories of the diffusing C atoms follow what was expected based on the observations in paper I with the C diffusing within the interface in the directions of the cell vectors of the BCC W. The calculated overall diffusion rate for the  $[10\bar{1}0]$ -I/ $[100]$  interface divided up into the diffusion pre-factor and the activation energy was estimated to be  $D_0 = 1.8 \times 10^{-8} \text{ m}^2/\text{s}$  and  $\Delta E = 1.24 \text{ eV}$  which well in line with the collection of elementary rates found in paper I.

The second area of focus involves the WC/W interfaces themselves and their properties as it relates to which interface combinations that can be expected to form most readily. In order to perform any large scale investigation into an unknown interface system such as this suitable tools must be available in order to leverage the amount of work that goes into it. As such a python package to search, build and analyze large sets of material interfaces was created named *interfaceBuilder* to facilitate this task. Using that package the work of adhesion and interfacial energies of 60,000 unique WC/W interfaces were calculated at 4 different relative translations using LAMMPS, a subset of interfaces were then re-calculated using VASP. The interfaces considered were the ones consisting of basal and prismatic type-I and type-II WC terminations against  $[100]$  and  $[110]$  BCC W terminations. The results showed a preference in interfacial energies for the  $[110]$  surfaces over the  $[100]$  surfaces in equivalent interfaces and showed the type-II prismatic terminations to be highly unfavourable. As expected the W terminations were preferred over the C terminations. The energetically preferred interfaces were, in order, the W terminated  $[10\bar{1}0]$ -I/ $[110]$  and  $[0001]$ / $[110]$  based on both the VASP and LAMMPS data.

Going forward it would be of interest to look at the other side of the WC/W interfaces, i.e. the W/workpiece interface. A relatively stable thickness of the BCC W would suggest some equilibrium between the removal of C and the removal of the BCC W layer. Whether this happens in a mechanical way with pieces being broken off once the thickness gets large enough or by being dissolved into the workpiece material with the equilibrium decided by the time

it takes the C to diffuse through the BCC W layer would be an important piece of information.

Further, it would be of interest to incorporate the values calculated for the diffusion into larger models to investigate if the experimentally observed wear rates could be described e.g. by the velocity of the WC/W phase boundary as C diffuses away from the WC towards the workpiece and how the thickness of the BCC W layer influences this velocity.

## 11. Acknowledgements

I would like to thank the people who have been involved in making this work possible starting with my main supervisor Prof. Rajeev Ahuja for giving me the opportunity to conduct this work within his group. Additionally I would like to thank my co-supervisors and collaborators for their insights and inputs along the way, Andreas Blomqvist, Martina Lattemann, Jonas Östby and Wei Luo as well as Bartek Kaplan for our early cooperation. This work was done in cooperation with Sandvik Coromant AB and I would like to thank them as well.

Beyond the strictly work related aspects of this kind of work I would like to extend a thank you to the people who have made this time enjoyable and indirectly help me in my work. John for the daily coffee breaks, my office mates for a large part of my time here, Cleber and Non, as well Rodrigo and José-Luis and the materials theory group. Finally a thank you to Torbjörn for the daily conversations regarding the pressing issues of our time, we may not have solved them but then again neither has anyone else.

## 12. Svensk Sammanfattning

Detta arbete fokuserar på nötning av hårdmetallskär och specifikt nötning vid svarvning av Ti-legeringar. Ti och Ti-legeringar används idag framförallt inom högteknologiska applikationer t.ex. inom flyg- och rymdindustrin, som bioimplantat eller inom kemikalieindustrin. Givet Ti-legeringars goda egenskaper när det kommer till hållfasthet i förhållande till vikt, styrka vid höga temperaturer och sin förmåga att klara korrosiva miljöer så är de möjliga applikationerna för Ti-legeringar många. Den begränsande faktorn är ofta priset, vilket tydliggörs av de avancerade applikationer inom vilka de används. En betydande del av priset kommer från bearbetningen av legeringarna. Detta grundar sig i att Ti har en mycket dålig värmeledningsförmåga samt att Ti är mycket reaktivt med det material som finns i de verktyg som används vid bearbetning. Dessa verktyg består av hårdmetall vilket är hårda WC korn i en mjukare matris oftast bestående av Co. Den dåliga värmeledningsförmågan leder till att temperaturen i kontakten mellan verktyget och arbetsstycket blir mycket hög och att verktygsmaterial diffunderar in i arbetsstycket. Experimentella studier har visat att det bildas ett tunt lager ren W på de yttersta WC kornen och detta kan endast hända genom att C diffunderar bort från kontakten.

I detta arbete ligger fokus på att undersöka de hastigheter med vilka C atomer kan röra sig ut från verktyget och in i det WC/W lager som visat sig existera. Arbetet fokuserar även på egenskaperna hos de uppkomna WC/W gränsytorna. Detta har gjorts med hjälp av simuleringar och problemet har angripits på ett flertal olika sätt.

I den första delen av detta arbete användes Densitetsfunktionalteori (DFT) för att undersöka den initiala diffusionen av C atomer ut från WC korn och in i WC/W gränsytor. Detta gjordes med metoderna Nudge Elastic Band (NEB), dimer-metoden och med Harmonic Transition State Theory (HTST). Med hjälp av dessa metoder och inom ramverket för DFT har diffunderingshastigheterna för C atomer som rör sig in i och inom WC/W gränsytor uppskattats för gränsytor innehållandes de två vanligast förekommande ytorna i WC material. Resultatet visade på lika hastigheter för diffusionen inom WC/W gränsytorna men på en stor skillnad mellan de två konfigurationerna när det gällde hastigheten för diffusion in i gränsytorna.

I den andra delen av detta arbete användes Molekylär Dynamik (MD) med parametriserade kraftfält för att kunna studera större system under längre tider än vad som är möjligt med DFT. Här undersöktes C diffusion i liknande WC/W gränsytor som i det första projektet men med betydligt större simuleringsceller. Fokus låg på att undersöka hur diffusionshastigheten påverkades

av hur mycket C som fanns kvar i det yttersta WC lagret. Resultatet visade att den mycket långsamma diffusionsprocess som verkar finnas i det initiala steget av C utarmningen ökar avsevärt när C atomer börjar försvinna från WC/W gränsytorna. Resultaten visade också att den stora skillnad som fanns mellan de två olika typerna av WC ytor till stor del försvann vid en C utarmningshalt motsvarande 50%.

I ett sista steg undersöktes C diffusionen i WC/W gränsytor med hjälp av kinetic Monte Carlo (kMC) modellering. I denna metod driver man systemet framåt ett händelsesteg i taget till skillnad från MD simuleringar där systemet som studeras drivs framåt i fasta tidssteg. Vilket händelsesteg som utförs bestäms av den sannolikhetsfördelning som finns för de tillgängliga processerna och efter att ett steg utförs simuleras sedan den tid detta steg har tagit. På detta vis kommer man runt den problematik som hindrar system med väldigt långsamma processer från att simuleras med MD som använts tidigare i arbetet. Detta gör också att de tidsskalor som kan simuleras oftast kan utökas avsevärt i förhållande till MD simuleringar. Baserat på kMC simuleringarna uppskattades förfaktorn för diffusion av C i WC/W gränsytan  $[10\bar{1}0]$ -I/ $[100]$  till  $1.8 \times 10^{-8} \text{ m}^2/\text{s}$  och diffusionsbarriären till 1.24 eV.

Vid sidan av C diffusionen har även egenskaperna hos olika WC/W gränsytor undersökts för att kunna förutsäga vilka typer av gränsytor som borde återfinnas i dessa tillämpningar. För att kunna göra detta konstruerades ett python paket, *interfaceBuilder*, för att kunna hantera stora samlingar av gränsytor och möjliggöra översiktliga beräkningar av dessa samt analysera dem på ett snabbt och smidigt sätt. Detta paket användes sedan för att skapa och beräkna WC/W gränsytors vidhäftningsenergi och gränsytsenergi för 60,000 unika gränsytor bestående av olika vanligt förekommande ytor i WC och W material. Baserat på gränsytsenergin bedöms de W terminerade gränsytorna  $[10\bar{1}0]$ -I/ $[110]$  och  $[0001]$ / $[110]$  vara de mest stabila.

# Bibliography

1. Ezugwu, E. & Wang, Z. Titanium alloys and their machinability - a review. *Journal of Materials Processing Technology* **68**, 262–274 (1997).
2. Ezugwu, E., Bonney, J. & Yamane, Y. An overview of the machinability of aeroengine alloys. *Journal of Materials Processing Technology* **134**, 233–253 (2003).
3. Kaur, M. & Singh, K. Review on titanium and titanium based alloys as biomaterials for orthopaedic applications. *Materials Science and Engineering: C* **102**, 844–862 (2019).
4. Zhanga, X., Chenb, Y. & Hu, J. Recent advances in the development of aerospace materials. *Progress in Aerospace Sciences* **97**, 22–34 (2018).
5. Saptaji, K., Gebremariam, M. A. & Azhari, M. A.B. M. Machining of biocompatible materials: a review. *International Journal of Advanced Manufacturing Technology* **97**, 2255–2292 (2018).
6. Rahman, M., Wong, Y. S. & Zareena, A. R. Machinability of Titanium Alloys. *JSME International Journal Series C* **46**, 107–115 (2003).
7. Pramanik, A. Problems and solutions in machining of titanium alloys. *International Journal of Advanced Manufacturing Technology* **70**, 919–928 (2014).
8. Krolczyk, G. M. *et al.* Ecological trends in machining as a key factor in sustainable production – A review. *Journal of Cleaner Production* **218**, 601–615 (2019).
9. Hartung, P. D. & Kramer, B. M. Tool Wear in Titanium Machining. *Annals of the CIRP* **31**, 75–80 (1982).
10. Dearnley, P. A. & Grearson, A. N. Evaluation of principle wear mechanisms of cemented carbides and ceramics used for machining titanium alloy IMI 318. *Materials Science and Technology* **2**, 47–58 (1986).
11. Odelros, S., Kaplan, B., Kritikos, M., Johansson, M. & Norgren, S. Experimental and theoretical study of the microscopic crater wear mechanism in titanium machining. *Wear* **376-377**, 115–124 (2017).
12. Kaplan, B., Odelros, S., Kritikos, M., Bejjani, R. & Norgren, S. Study of tool wear and chemical interaction during machining of Ti6Al4V. *International Journal of Refractory Metal & Hard Materials* **72**, 253–256 (2018).



13. Martin, R. M. *Electronic structure: Basic Theory and Practical Methods* (Cambridge University Press, 2004).
14. Koch, W. & Holthausen, M. C. *A Chemist's Guide to Density Functional Theory* (Wiley-VCH Verlag GmbH, 2001).
15. Kresse, G. & Hafner, J. Ab initio molecular dynamics for liquid metals. *Physical Review B* **47**, 558–561 (1993).
16. Kresse, G. & Furthmüller, J. Efficiency of ab-initio total energy calculations for metals and semiconductors using a plane-wave basis set. *Computational Materials Science* **6**, 15–50 (1996).
17. Kresse, G. & Furthmüller, J. Efficient iterative schemes for ab initio total-energy calculations using a plane-wave basis set. *Physical Review B* **54**, 11169 (1996).
18. Henkelman-group. *VTST-Tools 3.2* <http://theory.cm.utexas.edu>. University of Texas, Austin.
19. Born, M. & Oppenheimer, R. J. Zur Quantentheorie der Molekeln. *Annalen der Physik* **389**, 457–484 (1927).
20. Hohenberg, P. & Kohn, W. Inhomogeneous Electron Gas. *Physical Review* **136**, 864–871 (1964).
21. Kohn, W. & Sham, L. J. Self-Consistent Equations Including Exchange and Correlation Effects. *Physical Review* **140**, 1133–1138 (1965).
22. Bloch, F. Bemerkung zur Elektronentheorie des Ferromagnetismus und der elektrischen Leitfähigkeit. *Zeitschrift für Physik* **57**, 545–555 (1929).
23. Dirac, P. Note on Exchange Phenomena in the Thomas Atom. *Mathematical Proceedings of the Cambridge Philosophical Society* **26**, 376–385 (1930).
24. Ceperley, D. M. & Alder, B. J. Ground State of Electron Gas by a Stochastic Method. *Physical Review Letters* **45**, 566–569 (1980).
25. Becke, A. D. Density-functional exchange-energy with correct asymptotic behavior. *Physical Review A* **38**, 3098–3100 (1988).
26. Perdew, J. P. & Wang, Y. Accurate and simple analytic representation of the electron-gas correlation energy. *Physical Review B* **45**, 13244–13249 (1992).
27. Perdew, J. P., Burke, K. & Ernzerhof, M. Generalized Gradient Approximation Made Simple. *Physical Review Letters* **77**, 3865 (1996).
28. Hamann, D. R., Schlüter, M. & Chiang, C. Norm-conserving pseudopotentials. *Physical Review Letters* **43**, 1494–1497 (1979).
29. Blöchl, P. E. Generalized separable potentials for electronic-structure calculations. *Physical Review B* **41**, 5414–5416 (1990).

30. Vanderbilt, D. Soft self-consistent pseudopotentials in a generalized eigenvalue formalism. *Physical Review B* **41**, 7892 (1990).
31. Blöchl, P. E. Projector augmented-wave method. *Physical Review B* **50**, 17953 (1994).
32. Hellmann, H. Zur Rolle der kinetischen Elektronenenergie für die zwischenatomaren Kräfte. *Zeitschrift für Physik* **85**, 180–190 (1933).
33. Feynman, R. Forces in molecules. *Physical Review* **56**, 340–343 (1939).
34. Plimpton, S. Fast parallel algorithms for short-range molecular dynamics. *Journal of Computational Physics* **117**, 1–19 (1995).
35. Jones, J. E. On the Determination of Molecular Fields. II. From the Equation of State of a Gas. *Proceedings of the Royal Society of London* **106**, 463–477 (1924).
36. LAMMPS. *MD Bench marks* <https://lammps.sandia.gov/bench.html> (2019).
37. Juslin, N. *et al.* Analytical interatomic potential for modeling nonequilibrium processes in the W-C-H system. *Journal of Applied Physics* **98** (2005).
38. Tersoff, J. Empirical Interatomic Potential for Carbon, with Applications to Amorphous Carbon. *Physical Review Letters* **61**, 2879–2882 (1988).
39. Brenner, D. W. Empirical potential for hydrocarbons for use in simulating the chemical vapor deposition of diamond films. *Physical Review B* **42**, 9458–9471 (1990).
40. Brenner, D. W. *et al.* A second-generation reactive empirical bond order (REBO) potential energy expression for hydrocarbons. *Journal of Physics: Condensed Matter* **14**, 783–802 (2002).
41. Allen, M. P. *Introduction to Molecular Dynamics Simulation* (eds Attig, N., Binder, K., Grubmüller, H. & Kramer, K. D.) (John von Neumann Institute for Computing, Jülich, 2004).
42. Verlet, L. Computer experiments on classical fluids. i. thermodynamical properties of Lennard-Jones molecules. *Physical Review* **159**, 98–103 (1967).
43. Verlet, L. Computer experiments on classical fluids. ii. equilibrium correlation functions. *Physical Review* **165**, 201–214 (1968).
44. Voter, A. F. *Introduction to the Kinetic Monte Carlo Method in Radiation Effects in Solids* (eds Sickafus, K. E., Kotomin, E. A. & Uberuaga, B. P.) (Springer Netherlands, Dordrecht, 2007), 1–23.
45. Norris, J. R. *Markov Chains* (Cambridge University Press, 1997).
46. Pedersen, A., Henkelman, G., Schiøtz, J. & Jónsson, H. Long time scale simulation of a grain boundary in copper. *New Journal of Physics* **11**, 19 (2009).

47. Chill, S. T. *et al.* EON: software for long time simulations of atomic scale systems. *Modelling and Simulation in Materials Science and Engineering* **22**, 1–16 (2014).
48. Mehrer, H. *Diffusion in Solids* (Springer-Verlag Berlin Heidelberg, 2007).
49. Vineyard, G. H. Frequency Factors and Isotope Effects In Solid State Rate Processes. *Journal of Physics and Chemistry of Solids* **3**, 121–127 (1957).
50. Jónsson, H., Mills, G. & Jacobsen, K. W. Nudged Elastic Band Method for Finding Minimum Energy Paths of Transitions in Classical and Quantum Dynamics in Condensed Phase Simulations. *World Scientific*, 385 (1998).
51. Henkelman, G. & Jónsson, H. Improved tangent estimate in the nudged elastic band method for finding minimum energy paths and saddle points. *Journal of Chemical Physics* **113**, 9978–9985 (2000).
52. Henkelman, G., Uberuaga, B. P. & Jónsson, H. A climbing image nudged elastic band method for finding saddle points and minimum energy paths. *Journal of Chemical Physics* **113**, 9901–9904 (2000).
53. Henkelman, G. & Jónsson, H. A dimer method for finding saddle points on high dimensional potential surfaces using only first derivatives. *Journal of Chemical Physics* **111**, 7010–7022 (1999).
54. Malek, R. & Mousseau, N. Dynamics of Lennard-Jones clusters: A characterization of the activation-relaxation technique. *Physical Review E* **62**, 7723 (2000).
55. Kim, C.-S., Massa, T. R. & Rohrer, G. S. Interface Character Distributions in WC–Co Composites. *Journal of the American Ceramic Society* **91**, 996–1001 (2008).
56. Lay, S., Donnadieu, P. & Loubradou, M. Polarity of prismatic facets delimiting WC grains in WC-Co alloys. *Micron* **41**, 472–477 (2010).
57. Qian, G.-X., Martin, R. M. & Chadi, D. J. First-principles study of the atomic reconstructions and energies of Ga- As-stabilized GaAs(100) surfaces. *Physical Review B* **38**, 7649–7663 (1988).
58. Siegel, D. J., Jr., L. G. H. & Adams, J. B. Adhesion, stability, and bonding at metal/metal-carbide interfaces: Al/WC. *Surface Science* **498**, 321–336 (2002).
59. Reuter, K. & Scheffler, M. Composition, Structure, and Stability of RuO<sub>2</sub>(110) as a Function of Oxygen Pressure. *Phys. Rev. B* **65**, 035406 (2001).
60. Christensen, M. & Wahnström, G. Co-phase penetration of WC(10 $\bar{1}$ 0)/WC(10 $\bar{1}$ 0) grain boundaries from first principles. *Physical Review B* **67**, 115415 (2003).

61. García, J., Ciprés, V. C., Blomqvist, A. & Kaplan, B. Cemented carbide microstructures: a review. *International Journal of Refractory Metal & Hard Materials* **80**, 40–68 (2019).
62. Thermo-Calc Software. *TC Binary Solutions V1.1* 2019-03-25.
63. Banerjee, D. & Williams, J. C. Perspectives on Titanium Science and Technology. *Acta Materialia* **61**, 844–879 (2013).
64. Hua, J. & Shivpuri, R. A cobalt diffusion based model for predicting crater wear of carbide tools in machining titanium alloys. *Journal of Engineering Materials and Technology* **127**, 136–144 (2005).
65. Jianxin, D., Yousheng, L. & Wenlong, S. Diffusion wear in dry cutting of Ti–6Al–4V with WC/Co carbide tools. *Wear* **265**, 1776–1783 (2008).
66. Bermingham, M. J., Kirsch, J., Sun, S., Palanisamy, S. & Dargusch, M. S. New observations on tool life, cutting forces and chip morphology in cryogenic machining Ti-6Al-4V. *International Journal of Machine Tools & Manufacture* **51**, 500–511 (2011).
67. Zhang, S., Li, J. F., Deng, J. X. & Li, Y. S. Investigation on diffusion wear during high-speed machining Ti-6Al-4V alloy with straight tungsten carbide tools. *International Journal of Advanced Manufacturing Technology* **44**, 17–25 (2009).
68. Hatt, O., Crawforth, P. & Jackson, M. On the mechanism of tool crater wear during titanium alloy machining. *Wear* **374–375**, 15–20 (2017).
69. Stradi, D., Jelver, L., Smidstrup, S. & Stokbro, K. Method for determining optimal supercell representation of interfaces. *Journal of Physics: Condensed Matter* **29**, 1–7 (2017).
70. QuantumWise A/S. *Virtual NanoLab 2017.0* (www.quantumwise.com).
71. Nosé, S. A unified formulation of the constant temperature molecular dynamics methods. *Journal of Chemical Physics* **81**, 511–519 (1984).
72. Hoover, W. G. Canonical dynamics: Equilibrium phase-space distributions. *Physical Review A* **31**, 1695–1697 (1985).
73. *interfaceBuilder* <https://github.com/Eddddan/interfaceBuilder.git> (2021).
74. Momma, K. & Izumi, F. VESTA: a three-dimensional visualization system for electronic and structural analysis. *Journal of Applied Crystallography* **41**, 653–658 (2008).



# Acta Universitatis Upsaliensis

*Digital Comprehensive Summaries of Uppsala Dissertations  
from the Faculty of Science and Technology 2016*

Editor: The Dean of the Faculty of Science and Technology

A doctoral dissertation from the Faculty of Science and Technology, Uppsala University, is usually a summary of a number of papers. A few copies of the complete dissertation are kept at major Swedish research libraries, while the summary alone is distributed internationally through the series Digital Comprehensive Summaries of Uppsala Dissertations from the Faculty of Science and Technology. (Prior to January, 2005, the series was published under the title "Comprehensive Summaries of Uppsala Dissertations from the Faculty of Science and Technology".)

Distribution: [publications.uu.se](http://publications.uu.se)  
urn:nbn:se:uu:diva-434522



ACTA  
UNIVERSITATIS  
UPSALIENSIS  
UPPSALA  
2021